

The 2015–2017 Pamir Earthquake Sequence: Fore-, Main-, and Aftershocks, Seismotectonics and Fault Interaction

Wasja Bloch^{1,1,1}, Sabrina Metzger^{2,2,2}, Bernd Dieter Schurr^{3,3,3}, Xiaohui Yuan^{3,3,3}, Lothar Ratschbacher^{4,4,4}, Sanaa Reuter^{4,4,4}, Qiang Xu^{5,5,5}, Junmeng Zhao^{5,5,5}, Shohrukh Murodkulov^{6,6,6}, and Ilhomjon Oimuhammadzoda^{7,7,7}

¹Geoforschungszentrum Potsdam

²Helmholtz-Zentrum, Deutsches GeoForschungszentrum Potsdam

³Deutsches GeoForschungszentrum GFZ

⁴Geologie, Technische Universität Bergakademie Freiberg, 09599 Freiberg, Germany

⁵Institute of Tibetan Plateau Research, Chinese Academy of Sciences

⁶Institute of Geology, Earthquake Engineering and Seismology of the Academy Science of the Republic of Tajikistan

⁷Tajikistan Academy of Sciences

November 30, 2022

Abstract

A sequence of three strong (Mw7.2–6.4) and several moderate (Mw4.4–5.7) earthquakes struck the Pamir Plateau and surrounding mountain ranges of Tajikistan, China, and Kyrgyzstan in 2015–2017. With a local seismic network in operation in the Xinjiang province since August 2015, an aftershock network on the Pamir Plateau of Tajikistan since February 2016, and additional permanent regional seismic stations, we were able to record the succession of the fore-, main-, and aftershock sequences at local distances with good azimuthal coverage. We located 11,784 seismic events and determined the moment tensor for 35 earthquakes. The seismicity delineates the major tectonic structures of the Pamir, i.e., the thrusts that absorb shortening along the Plateau thrust front, and the strike-slip and normal faults that dissect the plateau into a westward extruding and a northward advancing block. Fault ruptures were activated subsequently at increasing distances from the initial Mw7.2 Sarez earthquake. All mainshock areas but the initial one exhibited foreshock seismicity which was not modulated by the occurrence of the earlier earthquakes. Modelling of the static Coulomb stress changes indicates that aftershock triggering occurred over distances of [?]90km on favourably oriented faults. The rupture of the second largest Mw6.6 Muji earthquake of the sequence happened despite its repeated stabilization through stress transfer in the order of -10 kPa. To explain the significant accumulation of Mw6+ earthquakes, we reason that the initial mainshock may have increased nearby fault permeability, and so facilitated fluid migration into the mature fault zones eventually triggering the later large earthquakes.

The 2015–2017 Pamir Earthquake Sequence: Fore-, Main-, and Aftershocks, Seismotectonics, Fault Interaction, and Fluid Processes

Wasja Bloch^{1,2*}, Sabrina Metzger¹, Bernd Schurr¹, Xiaohui Yuan¹,

Lothar Ratschbacher³, Sanaa Reuter³, Qiang Xu^{4,5}, Junmeng Zhao^{4,5},

Shokhrukh Murodkulov⁶, Ilhomjon Oimuhammadzoda⁷

¹ *GFZ German Research Centre for Geosciences, 14473 Potsdam, Germany*

² *Department of Earth, Ocean and Atmospheric Sciences, University of British Columbia, Vancouver V6T 1Z4, Canada*

³ *Geologie, Technische Universität Bergakademie Freiberg, 09599 Freiberg, Germany*

⁴ *Key Laboratory of Continental Collision and Plateau Uplift, Institute of Tibetan Plateau Research, Chinese Academy of Sciences, Beijing 100101, China*

⁵ *CAS Center for Excellence in Tibetan Plateau Earth Sciences, Beijing 100101, China*

⁶ *Institute of Geology, Earthquake Engineering and Seismology, National Academy of Sciences, Dushanbe, Tajikistan*

⁷ *Department of Geology under the Government of the Republic of Tajikistan, Dushanbe, Tajikistan*

27 June 2022

SUMMARY

A sequence of three strong (M_W 7.2, 6.4, 6.6) earthquakes struck the Pamir of Central Asia in 2015–2017. With a local seismic network, we recorded the succession of the fore-, main-, and aftershock sequences at local distances with good azimuthal coverage. We located 11,784 seismic events and determined 33 earthquake moment tensors. The seismicity delineates the tectonic structures of the Pamir in unprecedented detail, i.e., the thrusts that absorb shortening along the Pamir’s thrust front, and the strike-slip and normal faults that dissect the Pamir Plateau into a westward extruding block and a northward advancing block. Ruptures on the kinematically dissimilar faults were activated subsequently from the initial M_W 7.2 Sarez event at times and distances that follow a diffusion equation. All mainshock areas but the initial one exhibited foreshock activity, which was not modulated by the occurrence of the earlier earthquakes. Modeling of the static Coulomb stress changes indicates that aftershock triggering occurred over distances of ≤ 90 km on favorably oriented faults. The third event in the sequence, the M_W 6.6 Muji earthquake, ruptured despite its repeated stabilization through stress transfer in the order of -10 kPa. To explain the accumulation of $M_W > 6$ earthquakes, we reason that the initial mainshock may have increased nearby fault permeability, and facilitated fluid migration into the mature fault zones, eventually triggering the later large earthquakes.

Key words: Asia; Earthquake interaction, forecasting, and prediction; Seismicity and tectonics; Continental neotectonics; Dynamics: seismotectonics; Dynamics and mechanics of faulting;

1 INTRODUCTION

The Pamir occupies the northwestern tip of the India-Asia collision zone, where several major mountain belts—the Tian Shan, Kunlun Shan, Karakorum, and Hindu Kush—and two large depressions—the Tarim and Afghan-Tajik basins—converge (Fig. 1). It exhibits some of the highest strain rates for an intra-continental setting, both within the broad India-Asia collision zone and globally (Kreemer et al. 2014). Deformation involves shortening and dextral strike-slip shear along

* Corresponding author: wbloch@eoas.ubc.ca

its northern margin and sinistral strike-slip faulting and extension in its interior, the Pamir Plateau (Schurr et al. 2014).

On December 7, 2015, the moment magnitude $M_W 7.2$ Sarez sinistral strike-slip earthquake hit the Pamir interior. It ruptured three segments of the \sim NNE-striking Sarez-Karakul Fault System (SKFS) with a total length of ~ 80 km (Fig. 1a; Elliott et al. 2020; Metzger et al. 2017; Sangha et al. 2017). In the aftermath two $M_W > 6.4$ and multiple $M_W > 5$ earthquakes occurred on various segments of the nearby fault networks. Specifically, the June 26, 2016 $M_W 6.4$ Sary-Tash earthquake ruptured an \sim E-striking reverse fault below the Main Pamir Thrust System (MPTS; He et al. 2018), ~ 90 km NNE of the northern end of the Sarez rupture, and the November 25, 2016 $M_W 6.6$ Muji earthquake broke two segments of the \sim WNW-striking Muji Fault (Bie et al. 2018; Li et al. 2019, 2018), a dextral strike-slip fault ~ 30 km SW of the Sary-Tash earthquake (Figure 1a). Even for a region as seismically-active as the Pamir, this sequence was unusual: long-term earthquake bulletins (e.g., the Global Earthquake Model ISC-GEM; Di Giacomo et al. 2018; ISC 2021) report only 18 $M_W > 6.5$ earthquakes in the region between 1900 and 2015 (Figure 1b). The probability that the three recent $M_W > 6.4$ earthquakes occurred independently of each other, i.e., following a Poisson process, is 0.05%. Furthermore, the subsequent earthquakes showed a conspicuous activation pattern, with earthquakes occurring at increasing distances from the initial mainshock, on kinematically dissimilar fault zones, and over comparatively large distances (Video S1).

Earthquakes often occur in spatio-temporal clusters. Examples in the central Apennines, Italy (e.g., Chiaraluce et al. 2003, 2017; Michele et al. 2020; Valoroso et al. 2013), Southern California, United States of America (e.g., Chen et al. 2020; Freed & Lin 2001; Hauksson et al. 1993; Parsons & Dreger 2000; Toda & Stein 2020), Baluchistan, Pakistan (Yadav et al. 2012), the South Iceland Seismic Zone (e.g., Árnadóttir et al. 2003; Einarsson et al. 1981; Hreinsdóttir et al. 2009) or the Sunda Arc, Indonesia (e.g., Briggs et al. 2006; Pollitz et al. 2006; Wiseman & Burgmann 2011) demonstrate how sequences of earthquakes may unfold over time. Attempts to foresee the imminent occurrence of larger events during periods of seismic unrest encompass the estimation of elastic or viscoelastic Coulomb failure stress changes on adjacent fault segments (e.g., Chen et al. 2020; Lorenzo-Martín et al. 2006; Nalbant et al. 2005; Ryder et al. 2012; Stein 1999; Toda et al.

1998; Toda & Stein 2020; Wiseman & Burgmann 2011), and the detection of foreshock cascades (e.g., Chen et al. 2020; Ellsworth & Bulut 2018; Schurr et al. 2020). Sometimes, fluids escape from an activated fault network and induce fault slip (Hamling & Upton 2018), but unambiguous identification of large earthquakes being triggered by increased fluid pressure is restricted to controlled injection experiments (e.g., Ellsworth et al. 2019; Woo et al. 2019). In any case, investigations of fault interactions in earthquake sequences require intimate knowledge about the structure of the involved fault segments (e.g., Mildon et al. 2019).

Since August 2015, we had a temporary seismic network in operation in the eastern Pamir in the Xinjiang province of China. It recorded the initial December 2015 Sarez earthquake (Fig. 1a). In February 2016, we deployed a network on the Pamir Plateau of Tajikistan in the vicinity of the Sarez earthquake rupture. The combined networks recorded then both the June 2016 Sary-Tash and the November 2016 Muji earthquake sequences with a very good azimuthal coverage. Additional moderate earthquakes with their own fore- and aftershock sequences augmented the seismotectonic record.

After introducing the neotectonic framework (Section 2), the dataset, and the methodology (Section 3), we document the spatio-temporal fore-, main-, and aftershock patterns (Section 4). We then use the obtained moment tensors and precise seismic event locations to determine the location, orientation, kinematics, and activation times of the seismically active structures in the Pamir and southern Tian Shan region, associate them with geologically mapped faults, and evaluate their seismic history. To identify long-term seismicity patterns, we compare our findings with the results of an earlier experiment (Section 5; Schurr et al. 2014; Sippl et al. 2013b). We construct a Coulomb stress-transfer model that honors the spatio-temporal seismic activation patterns and aseismic displacements inferred from interferometric synthetic-aperture radar (InSAR) to investigate processes of earthquake interaction and nucleation (Section 6). The combined results allow us to reason about the possible involvement of co-seismically mobilized fluids in fault activation (Section 7).

2 NEOTECTONIC FRAMEWORK

In the Pamir, northward displacement at rates of 13–19 mm/yr is currently accommodated along its margins by (i) crustal shortening along the MPTS—which yielded the June 2016 earthquake—in the north, in particular the Pamir Frontal Thrust, (ii) the sinistral Darvaz Fault Zone in the west and northwest, (iii) the dextral Karakorum Fault System in the southeast, and (iv) the Kongur Shan-Taxkorgan Normal Fault System in the Chinese eastern Pamir (Fig. 1; e.g., Chevalier et al. 2015; Ischuk et al. 2013; Jade et al. 2004; Metzger et al. 2020; Schurr et al. 2014; Zubovich et al. 2010, 2016). The Karakorum Fault System probably links with the Sarez-Murghab Thrust System via the Aksu-Murghab Fault Zone on the Pamir Plateau (Robinson 2009; Rutte et al. 2017). The dextral transpressive Kashgar-Yecheng Fault System (Cowgill 2009) linked shortening in the western Kunlun Shan with that along the MPTS; since ~ 5 Ma (Sobel et al. 2011) and up to now (Zubovich et al. 2010), the Pamir and the Tarim basin have been moving north at about the same rate, rendering the transform component mostly inactive. The Muji Fault—that yielded the November 2016 earthquake—links \sim E-W extension along the Kongur Shan Normal Fault System to the MPTS (Li et al. 2019; Schurr et al. 2014; Sippl et al. 2014). The Kongur Shan Normal Fault System has accommodated ≥ 35 km of \sim E-W extension, mostly since ~ 7 Ma (Robinson et al. 2004, 2007; Thiede et al. 2013); extension and dextral strike-slip along the Muji Fault are ongoing, as implied by seismicity and the divergence of the Global Navigation Satellite System (GNSS) velocity field between Pamir’s interior and the Tarim block (Li et al. 2019; Zubovich et al. 2010).

In the interior of the Pamir, the active displacement field is composed of bulk northward movement combined with \sim E-W extension (Zhou et al. 2016; Ischuk et al. 2013). The crust hosts sinistral strike-slip faulting on \sim NE-striking planes, dextral strike-slip faulting on conjugate planes, and—to a lesser degree—normal faulting on \sim N-striking planes (Schurr et al. 2014). In the interior of the eastern Pamir the lack of significant seismicity demonstrates that it is moving northward en bloc; this agrees with the GNSS data. The only \sim NE-striking sinistral-transpressive fault system of the Pamir interior, which has a clear morphologic expression and is seismically active, is the SKFS, which yielded the initial December 2015 earthquake. It stretches from south of Lake Sarez

to north of Lake Karakul (Elliott et al. 2020; Metzger et al. 2017; Schurr et al. 2014; Strecker et al. 1995). The northern SKFS is interpreted as a horst-graben structure (Nöth 1932; Strecker et al. 1995), the southern SKFS currently shows dominant sinistral strike-slip and subordinate normal displacements (Elliott et al. 2020; Metzger et al. 2017). Its southward continuation is the proposed source structure of an $M_W \sim 7.3$ earthquake that hit the Pamir in 1911 (Fig. 1b; Kulikova et al. 2016; Elliott et al. 2020). The \sim E-W extension—increasing into the western Pamir—is driven by westward gravitational collapse of thickened Pamir-Plateau crust into the Tajik Depression (Metzger et al. 2020; Schurr et al. 2014; Stübner et al. 2013).

Beneath the Pamir, Asian lithosphere forms a $\sim 90^\circ$ arc that is retreating northward and westward as traced by intermediate-depth seismicity (60–300 km; Schneider et al. 2013; Sippl et al. 2013a). Kufner et al. (2016) and Bloch et al. (2021) inferred that the Asian slab retreat is forced by indentation of Indian lithosphere, bulldozing into the lithosphere of the Tajik-Tarim basin at mantle depth. In this context, the SKFS and the two largest earthquakes in the Pamir interior—the December 2015 and the 1911 earthquakes—with similar sinistral strike-slip mechanisms in about the same region, likely express the underthrusting of the northwestern leading edge of the Indian mantle lithosphere indenter. The 2015 Sarez rupture may be the most recent manifestation of the shear zone at the northwestern tip of the indenter, building a continuous fault zone along the indenter’s western edge and connecting the distributed sinistral fault zones of the Hindu Kush with the SKFS (Kufner et al. 2018, 2021; Metzger et al. 2017; Schurr et al. 2014).

3 SEISMOLOGICAL DATA AND METHODS

3.1 Data

We operated the East Pamir seismic network (FDSN code 8H; Yuan et al. 2018a) with 30 sites in the eastern Pamir, northwestern Kunlun, and northwestern Tarim Basin between August 2015 and July 2017, and the Sarez-Pamir aftershock seismic network (FDSN code 9H; Yuan et al. 2018b) with 10 sites on the Pamir Plateau between February 2016 and July 2017 (Fig. 1a). We used additional seismic waveform data from the Xinjiang regional seismic network (SEISDMC 2021) and the Tajik National Seismic Network (FDSN code TJ; PMP International (Tajikistan) 2005).

We detected 39,309 seismic events using the *Lassie* earthquake detector as coherent peaks in move-out corrected, smoothed, pulse-like seismogram image functions that were stacked on a rectangular grid of $100 \times 100 \times 10$ trial subsurface points with a spacing of $10 \times 10 \times 30$ km (Comino et al. 2017) using the 1-D velocity model of Sippl et al. (2013b). The initial location and predicted P- and S-wave arrival times were used as a starting point for phase arrival time picking. We picked P-wave arrival times automatically with *MannekenPix* (Aldersons 2004), where *obspy*'s STA/LTA triggers and predicted arrivals from the detection routine were used as starting points; S-wave arrival times were picked with *spicker* (Diehl et al. 2009). Filter window lengths and positions for both algorithms were calibrated with manually picked phase arrivals of 59 events. After each picking run, events were located with *hypo71* (Lee & Lahr 1972), and arrival times with the highest residuals were removed until the location root-mean-square (RMS) misfit fell below a threshold of 2 s for P-waves and 3 s for P- and S-waves combined. We then used a subset of 1,855 seismic events with the best constrained arrival-time picks to invert for a 1-D velocity model and static station corrections using *velest* (Kissling et al. 1994). We removed arrival times that yielded a residual 5 times larger than the standard deviation of all residuals of a certain seismic phase on a certain station, resulting in preliminary locations for 29,795 events. We excluded 20 apparent high-RMS misdetections (e.g., teleseismic events or network-wide null data in the XJ network), 13,149 events with less than 6 arrival time picks, 9,366 events with an azimuthal gap larger than 270° and 810 events below 300 km depth. Some events were removed due to more than one criterion. We manually revised the picks of 82 events of special interest, such as mainshocks or major foreshocks. After this step, we located 11,782 seismic events in the 3-D P-wave velocity model of Bloch et al. (2021) with *simulps* (Thurber 1983). We computed waveform cross-correlation differential arrival times of event pairs less than 10 km apart with *obspy* (Krischer et al. 2015) and determined refined relative event locations for 3,748 events using differential P- and S-wave catalog- and cross-correlation-arrival-times in *hypoDD* (Figs. S1 to S3; Waldhauser & Ellsworth 2000). The depth of 2,352 likely shallow events could not be resolved. They are located at the surface (i.e., the top boundary of the velocity model at -3 km); their map view distribution is sim-

ilar to events with well-constrained depths, giving us confidence that they do not bias the overall seismicity pattern (Bloch et al. 2022).

3.2 Regional Moment Tensors

We determined regional moment tensors using the *RMT* algorithm of Nábělek & Xia (1995). Green’s functions were computed with the discrete wavenumber summation method of Bouchon (1981) from the velocity and damping structure, previously obtained by Sippl et al. (2013b) (Fig. S4). Seismograms were band-pass filtered per event at lowest possible frequencies still providing good signal. For most events, filter corners of 20 and 60 s were suitable. Only events 2, 5, and 7 (Tab. 1) were filtered with a broader pass band between 15 and 80 s, and events 1, 3, and 7 with a narrower one between 10 and 40 s. Noisy waveforms were discarded interactively. We allowed small timing adjustments between observed and synthetic seismograms to match the phase. In total, we were able to retrieve 33 moment tensors of events with moment magnitude M_W between 4.0 and 6.0 (Tab. 1; Bloch et al. 2022). Moment tensors of the three large mainshocks could not be computed due to clipped waveforms; we instead report the moment tensor and magnitude published by the National Earthquake Information Center (NEIC).

A comparison between moment tensors and magnitudes of 10 events that were also analyzed by NEIC shows that the focal mechanisms agree (Fig. S5a). Significant differences occur only for two events from the Sary-Tash aftershock sequence (8 and 11 in Figure S5a). Within the context of other similar mechanisms in the sequence, the good waveform fit (Fig. S6 and S7), and given our better database, we are confident in our solutions.

3.3 Magnitudes

Calibrated local magnitudes M_L were obtained for all events by investigating the largest horizontal ground displacement amplitude A as a function of distance R . Following Bormann & Dewey (2012), we corrected the seismograms for their respective instrument response function and convolved them with the one of a Wood-Anderson seismograph. We measured the largest amplitude of

any of the horizontal components and calibrated the magnitude–amplitude–distance relationship (Bormann & Dewey 2012):

$$M_L^i = \log_{10} A^i + B \log_{10} R^i + CR^i + D \quad (1)$$

by minimizing:

$$\epsilon = \frac{1}{N} \sum_{i=1}^N \sqrt{(M_L^i - M_W^i)^2} \quad (2)$$

for all 921 station observations i of the 33 events for which M_W is available (Fig. S5c). We report the so calibrated M_L as the mean value of M_L^i after removal of outliers.

We computed the magnitude of completeness M_c of the entire catalog as the lower end of the longest linear segment of the cumulative frequency–magnitude distribution (Fig. S5d). A daily minimum completeness magnitude M_c^{min} was computed as the most frequent magnitude (binned in intervals of 0.1) observed in the previous 60 days (Woessner & Wiemer 2005).

4 SEISMICITY

Fig. 2 shows different representations of the spatio-temporal seismicity pattern. In the following, regions of distinct seismic activity are denoted with capital letters A – I . They are defined as rectangular areas around the three largest mainshock fault zones (A , C , E) and 15 km radii around the more moderate mainshocks (B , D , F – I) down to 50 km depth (Fig. 2a). The largest earthquake within each volume, specifically its hypocentral location and time, is denoted with an asterisk (A^* – I^*). Foreshocks are events that occurred in the so-defined volumes before the respective mainshock. Important foreshocks are denoted with a prime symbol (c' and e').

Seismicity in the studied time period was high and modulated by the occurrence of the three major earthquakes, which mark peaks in the detected earthquake rate (Figs. 2b and 2c; Video S1) at an overall magnitude of completeness $M_c = 2.3$ (Fig. S5d). The Sarez mainshock A^* and early aftershocks occurred when only the 8H seismic network was in operation. Hence, the magnitude of completeness was relatively high in the mainshock area ($M_c^{min} \approx 2.5$, Fig. 2d), compared to the eastern Pamir and Tarim basin area ($M_c^{min} \approx 1.6 - 2$). The installation of the 9H network in February 2016 on the Pamir Plateau increased the sensitivity of the entire network significantly

($M_c^{min} \approx 1.8$), even though high aftershock productivity deteriorated the detection threshold at times ($M_c^{min} \approx 2.2$). Other peaks in the event rate are due to the largest aftershock of the Sarez earthquake (B^*), an earthquake swarm in the western Pamir (D), and M_W 4–5 earthquakes near Yarkant (F^*), Khorog (G^*), Karamyk (H^*), and Taxkorgan (I^* ; Figs. 2a and 2c; Tab. 1).

The mainshocks B^* – H^* following the Sarez earthquake sequentially activated fault zones at increasing epicentral distance r from the centroid location of the Sarez earthquake (Fig. 2e, S8). The time of the fault activation is approximately enclosed in an envelope function of the form of a diffusion equation (Shapiro et al. 2003, 1997):

$$r = r_0 + \sqrt{2\pi D(t - t_0)}, \quad (3)$$

where r_0 is the distance from the Sarez centroid to the northern or southern end of the rupture, t_0 is the main shock origin time (Tab. 1) and D is a scaling constant that may be interpreted as hydraulic diffusivity. The sequential activation is not observed in the foreshock activity (Figs. 2c and 2e). The fault volumes A , B , C , D , E , and G were seismically active before the respective mainshocks—even years before, as recorded by the local TIPAGE seismic network (Schurr et al. 2014). This makes the distinction between foreshocks and background seismic activity only possible in retrospect. It is also not evident that the foreshock activity was triggered, enhanced, or diminished by any mainshock. Some rupture volumes showed phases of increased foreshock activity (C in February and April 2016, E in May and August 2016; Fig. 2c) and aftershock rates (C in August 2016, E in February 2017; Fig. S9). However, these phases do not correlate spatially, but rather represent subordinate aftershock sequences. Only volume B of the largest Sarez aftershock, which occurred ~ 25 km from the Sarez epicenter, started to become seismically active immediately after the Sarez mainshock.

Crustal seismicity that is not associated with any of the mainshocks delineates known neotectonic structures (Figs. 1, 2a, and 3): the MPTS exhibited diffuse seismic activity; the Kongur Shan Normal Fault System was seismically active between the Muji Fault and the northern end of the Taxkorgan Fault; the Aksu-Murghab Fault Zone was active along a swath in the south-central Pamir. In the following, we investigate the mainshock volumes, providing a detailed seismotectonic framework for the active deformation field of the Pamir.

5 SEISMOTECTONICS

5.1 Sarez Earthquake

The 2015 $M_W7.2$ Sarez earthquake (A^* in Figs. 2 and 4; Tab. 1) ruptured an ~ 80 km long part of the SKFS between Lake Sarez and the Kokujbel Valley south of Lake Karakul (Figs. 3 and 4; Elliott et al. 2020; Metzger et al. 2017; Sangha et al. 2017). Metzger et al. (2017) divided the rupture plane into three segments distinguished by strike changes (Fig. 4a). The northern part of the southern segment showed swarm-like seismic activity with 290 events detected during the August 2008 to July 2010 TIPAGE deployment (Fig. 4b; Sippl et al. 2013b). The swarm had ceased in August 2015, with only one $M_L2.4$ event detected on the fault in the 4 months before the Sarez mainshock (Fig. 4b, ~ 20 km from the hypocenter). The relative seismic quiescence before the mainshock and a magnitude of completeness $M_c^{min} \approx 2.0 - 2.5$ (Figs. 2c-d) suggests that no significant foreshock occurred before the Sarez earthquake.

The aftershocks of the Sarez earthquake skirted around the co-seismic slip patch, with a concentration at the northern end of the rupture (Fig. 4c; ~ 60 km from the hypocenter) and with sinistral transtensional focal mechanisms (Fig. 4a). Aftershocks also concentrated ~ 20 km south of the end of the co-seismically active fault patch (Fig. 4c; -30 km), where the largest $M_W5.3$ aftershock B^* with a sinistral strike-slip mechanism similar to the Sarez mainshock occurred 102 days after the mainshock; it spawned its own aftershock series (Figs. 2c, 3, and 4d). An area of relative seismic quiescence between the southern end of the Sarez rupture and aftershock B^* (between 10 and 30 km south of the Sarez hypocenter A^* , Fig. 4d) may be attributed to the 1918 $M_W6.6$ earthquake that could have relaxed this segment (Fig. 1b; Bondár et al. 2015).

The associated moment tensors exhibit both sinistral strike-slip and normal faulting mechanisms. Neither the co- nor the post-seismic activity reactivated the $\sim E$ -striking, Cenozoic thrusts and normal faults of this part of the Pamir (Fig. 4a). The $\sim NNE$ -strike of the normal-fault nodal planes are parallel to the many tensional surface-breaks mapped on ground along the northern segment (Figure 6 of Metzger et al. 2017) and the Quaternary-filled grabens, outlined on the 1:200,000 geological maps and traceable from topography (Figure 4a; Yushin et al. 1964). An important event

of the earthquake sequence was the April 9, 2016 M_W 4.1 dextral strike-slip event c' that occurred 124 days after the Sarez mainshock, \sim 85 km north of the tip of its rupture plane, and 78 days before and \sim 10 km east of the hypocenter of the Sary-Tash earthquake (Figs. 2c, 4d, and 5).

5.2 Sary-Tash Earthquake

The Sary-Tash earthquake (C^* in Figs. 2, 3, 4, and 5; Tab. 1) occurred within the MPTS, westerly adjacent to the 2008 M_W 6.6 Nura earthquake (Schurr et al. 2014; Sippl et al. 2014; Teshebaeva et al. 2014; Qiao et al. 2015). The region—geologically poorly-mapped in the high-altitude terrain of the Tajikistan-Kyrgyzstan-China border triangle—is characterized by a complex network of faults with both \sim N- and \sim S-dips, making the choice of the fault plane from the two nodal planes non-trivial. NEIC reports a comparatively low double-couple component for the mainshock moment tensor of 86%, hinting at the complexity of the rupture process.

The earthquake volume partially overlaps with the aftershock volume of the 2008 Nura earthquake (Sippl et al. 2014) and was seismically active throughout the different deployment periods of the various seismic networks covering the region; 13 small earthquakes (M_L 1.6–3.7) were detected in the vicinity of the future Sary-Tash earthquake in the two months preceding the 2008 Nura earthquake during the TIPAGE deployment and 188 (M_L 1.0– M_W 4.4) in the 11 months before the Sary-Tash earthquake since the 8H network was active (Figs. 2c, 5c and 5d). Foreshock activity was high compared to the Sarez and Muji sequences and peaked in three \sim 1-month-long swarms in March, April, and June 2016 (Fig. 2c). Notably, the events that followed the April 9, 2016 foreshock c' concentrated around the future hypocenter C^* in along-strike view (Fig. 5c). The aftershocks of the Sary-Tash earthquake outlined an about vertical, \sim E-striking structure to \sim 20 km depth east of the hypocenter (Figs. 5b and 5e). Moment tensors display a variety of focal mechanisms, again testifying to a complex fault-zone (Figs. 3 and 5a).

Fault-slip models of InSAR displacement maps slightly favor the steeply N-dipping nodal plane (FP1) over the gently \sim S-dipping one (FP2) for the Sary-Tash mainshock (He et al. 2018). If FP2 was the main fault plane, the aftershocks would crosscut it and be concentrated inside the volume of the largest slip (Fig. 5b). This is contrary to what is observed for the Sarez (Section 4.2.1)

and Muji (Section 4.2.3) earthquakes, and many other earthquakes worldwide, where aftershocks concentrate *around* the segments of highest slip (Das & Henry 2003). We prefer the \sim N-dipping FP1 as the main fault plane, because with this choice the aftershocks are located in the hanging wall and up-dip of the largest co-seismic slip (Fig. 5b), a pattern that has also been observed for the 2008 Nura earthquake (Sippl et al. 2014). The hypocenter is located at the western end of the geodetically-determined co-seismic slip patch (He et al. 2018), at 11.9 km depth, to the west and at 8.6 km hypocentral distance to the M_W 4.4 foreshock c' (Fig. 5e). The variable aftershock focal mechanisms tend to have dextral-transpressive mechanisms on \sim E-striking planes, except for two normal faulting events at the eastern end of the rupture (Fig. 5a). The \sim E-striking nodal planes of the strike-slip solutions are interpreted to carry the dextral strike-slip deformation identified in the background seismicity of the TIPAGE deployment data and by geological fault-slip analysis within the MPTS and in the Kyzilart Transfer Zone; even the normal-fault earthquakes, indicating E–W extension, have neotectonic fault equivalents, and were interpreted as interaction of the SKFS with the MPTS (Sippl et al. 2014). The hypocenter depth and presumed N-dip of the Sary-Tash earthquake fault suggest that a basement fault in the footwall of the Pamir Frontal Thrust got re-activated, as such faults are common in the Tian Shan immediately to the north (Figure 1b). In contrast, the 2008 Nura earthquake ruptured a \sim S-dipping plane; its hypocenter lay at 3.4 km depth and thus likely in the MPTS imbricate stack. That the Sary-Tash and Nura aftershock activities hardly overlap along strike, occupy different depth intervals, and differently-dipping patches indicate that they activated different faults (Figs. 5c and 5d). Another difference is that the shallow Nura earthquake re-activated several pre-existing NE- and NW-striking faults in the Tian Shan during its regionally-extensive aftershock sequence; the deeper Sary-Tash earthquake did not.

5.3 Muji Earthquake

153 days after the Sary-Tash earthquake, the M_W 5.0 foreshock to the Muji earthquake e' , and its mainshock E^* occurred on the Muji Fault, \sim 35 km southeast of the end of the rupture plane of the Sary-Tash earthquake. This configuration likely connects the MPTS in the area of the Sary-Tash earthquake with the Muji Fault along the Kyzilart Transfer Zone.

The rupture plane of the 2016 M_W 6.6 Muji earthquake (E^* in Figs. 2, 5, and 6; Tab. 1) broke nearly simultaneously in two main slip patches; a third slip patch, modeled below ~ 20 km depth, is unresolved (Bie et al. 2018). The area of the eastern slip patch was seismically active during the TIPAGE (2008–2010) and the current deployment (2015–2017; Fig. 6b). The M_W 5.0 Muji foreshock e' occurred only 12 minutes before the mainshock, at the western end of the rupture plane and at ~ 460 m hypocentral distance (Figs. 6a and 6b). We identified a series of four more foreshocks between e' and E^* in the seismogram of the closest station EP10 but could not locate them. The mainshock hypocenter was at 13.7 km depth. Aftershocks concentrated around and below the highest slip zone at the WNW end of the rupture plane, tightly constrained to the rim of the main slip patch; they continued ~ 10 km beyond its ESE' end of the eastern slip patch (Fig. 6c). The western continuation of the Muji fault remained seismically quiet.

Fore- and aftershock moment tensors exhibit dextral focal mechanisms similar to the mainshock. Notably, the two western focal mechanisms have a small reverse faulting component, while the two eastern ones have a small normal faulting component, a fault kinematic that was also observed in the morphology of the surface breaks (Li et al. 2019). This is compatible with the transition from the nearly purely extensional faulting along the Kongur Shan Normal Fault System to the dextral-transpressional Kyzilart Transfer Zone and MPTS.

The occurrence of aftershocks east but not west of the Muji mainshock rupture plane may suggest that the western continuation of the Muji Fault was not critically stressed. Either it was relaxed by the sinistral far-field strain of the 2008 Nura and 2016 Sary-Tash earthquakes or because it already slipped in an unrecorded earthquake or an undetected slip transient on the Kyzilart Transfer Zone. A candidate for an earthquake that filled this seismic gap is the 1974 Markansu earthquake (Fig. 1b). It has been located south of (Fan et al. 1994) and re-located (Sippl et al. 2014) on the Pamir Frontal Thrust, and full-waveform inversion suggests a complex thrust mechanism similar to the 2008 Nura earthquake (Langston & Dermengian 1981). But Burtman & Molnar (1993) advocated for a dextral strike-slip mechanism similar to the Muji earthquake which would be consistent with the expected slip sense on the quiet segment of the Muji fault. Alternatively, the fault segment with the seismic gap may creep aseismically.

5.4 Northwest Pamir Earthquake Swarm

An earthquake swarm of 80 events occurred on the western side of Pamir’s Academy of Sciences Range, hosting Pamir’s highest peaks (*D* in Figures 2 and 3; Tab. 1). It was active throughout the deployment of the Sarez aftershock network (Fig. 2c), with an activity peak, including the largest M_W 4.6 event *D**, in August 2016. Focal mechanisms indicate normal faulting on \sim N(NW)-striking planes. Well-located hypocenters and moment tensor centroids show that most seismicity clustered at shallow depth (≤ 6 km; Fig. 3). Such normal-faulting solutions are—together with strike-slip solutions—typical for the western Pamir, the part of the Pamir Plateau that shows westward-increasing gravitational collapse of crust into the Tajik Depression (Kufner et al. 2018; Schurr et al. 2014).

5.5 Yarkant Earthquake

On January 20, 2017, an M_W 5.0 earthquake occurred 53 km southwest of Yarkant, Xinjiang (*F** in Figs. 2 and 3; Tab. 1). Three events were detected in its volume *F* before the earthquake—one of them only 55 minutes before the mainshock—and a total of 41 aftershocks. The moment tensor indicates thrusting on either a shallowly- or a steeply-dipping fault plane. Seismicity aligns along a \sim N-striking structure (Fig. 3), paralleling the topographic slope and the strike of the shallowly-dipping nodal plane. We interpret these earthquakes to record top-to-NE thrusting along \sim SW-dipping faults, compatible with the growth of the eastern Pamir into the Tarim Basin (Figs. 1 and 3).

5.6 Khorog Earthquake

On March 22, 2017, an M_W 4.9 earthquake occurred ~ 51 km ENE of Khorog, Tajikistan (*G** in Figs. 2 and 3; Tab. 1). The volume *G* of the earthquake was active throughout the deployment of the 9H network with 24 seismic events detected before the mainshock. Whether the structure was activated by the Sarez earthquake—whose hypocenter is located ~ 90 km NE of the earthquake—is unclear, because of the limited sensitivity of the network before the 9H network deployment. Two \sim NE-trending streaks of seismicity can be identified in map view; the focal mechanism indicates

sinistral strike-slip on a \sim NE-striking fault. The depth of the earthquake is not well constrained due to the limited network coverage (Figure 3). The earthquake cluster lies along a fault zone classified as likely active by Stübner et al. (2013) and Schurr et al. (2014) due to linear topographic expressions; the fault zone coincides with the southeastern part of the Pathus-Nemos Fault of Strom (2014); it overprints the Miocene dextral-normal Gund shear/fault zone at an acute angle (Fig. 1b; Worthington et al. 2020). As a mappable continuation of the neotectonic fault network at the southern continuation of the SKFS (Fig. 1b), we interpret the Khorog earthquake cluster as part of the distributed faults that connect the SKFS with the sinistral fault zones of the Hindu Kush (e.g., the Chaman, Panjshir, Central Badakhshan Fault Zones; Fig. 1b), outlining a continuous fault zone along the western edge of the Indian indenter at mantle depth (Section 2; Metzger et al. 2017).

5.7 Karamyk Earthquake

An M_W 6.0 earthquake happened on May 3, 2017 near the Kyrgyz-Tajik border, \sim 25 km west of the settlement of Karamyk, Kyrgyzstan (H^* in Figs. 2 and 3; Tab. 1). The event was outside of the network, but due to the relatively large magnitude some aftershock seismicity could be located and the moment tensors of the mainshock and one aftershock could be determined. The seismicity outlined a \sim NE-trending cluster, with a dextral strike-slip- and a reverse-faulting focal mechanism for the mainshock and the aftershock, respectively (Figure 3). The cluster lies along a Cenozoic fault zone in the Tian Shan, outlined by partly overthrustured Jurassic-Paleogene basin strata; geological fault-slip analysis along the eastern strands of these fault zone reveals top-to-NW thrusting with a dextral strike-slip component (stations TS19 to TS22 in fig. S7 in Kufner et al. 2018).

5.8 Taxkorgan Earthquake

The last moderate earthquake detected during our recording period was the M_W 5.4 Taxkorgan earthquake on May 10, 2017, \sim 23 km south of Taxkorgan, Xinjiang (I^* in Figs. 2 and 3; Tab. 1). Aftershock seismicity and the focal mechanism indicate that it reactivated a steeply \sim ENE-

dipping segment of the Taxkorgan Normal Fault (Robinson et al. 2007). 14 foreshocks preceded the earthquake, half of them in the two months after the Muji earthquake (Figures 2 and 3). The Taxkorgan Normal Fault can be interpreted as part of the Kongur Shan–Taxkorgan Normal Fault System, with a southward decreasing amount of extension (Fig. 1).

5.9 Regional Stress Field

The tectonic interpretation resolved the nodal plane ambiguity of most moment tensors. We inverted the resultant slip vector orientations for the regional deviatoric unit stress tensor \hat{S} by minimizing the misorientation between the slip vector and the predicted largest shear stress on the fault plane, using the *slick* toolbox (Michael 1984, 1987). In north–east–down-convention:

$$\hat{S} = \begin{pmatrix} -0.798 & 0.596 & -0.004 \\ 0.596 & 0.867 & 0.177 \\ -0.004 & 0.177 & -0.069 \end{pmatrix} \quad (4)$$

The stress tensor indicates near-horizontal, N18°W-oriented compression σ_1 , N72°E-oriented extension σ_3 , and a 81° SW-plunging σ_2 (Fig. 3). The relative magnitudes of σ_1 , σ_2 , and σ_3 are -0.99, -0.09, and 1.08. The stress field is dominantly strike-slip with a reverse faulting component. σ_1 is about parallel to the GNSS vectors in the Pamir interior and σ_1 at mantle depth (Bloch et al. 2021). σ_2 has a compressional component, represented by the shape factor $\frac{\sigma_2 - \sigma_1}{\sigma_3 - \sigma_1} = 0.44$, or the compensated linear vector dipole component of the stress tensor of 17%. We interpret the vertical compression component to reflect the bulk thinning of the crust of the Pamir Plateau due to its westward (along the σ_3 -orientation) collapse into the Tajik Depression.

5.10 Discussion of Seismotectonic Processes

Tectonically, the earthquake sequence recorded between August 2015 and July 2017 outlines the first-order deformation field of the Pamir and southernmost Tian Shan. The northward displacement of the eastern Pamir Plateau, tied to the Tarim-Basin lithosphere, is absorbed to a large extent along the Pamir front, the MPTS. Basement-rooted faults of the Paleozoic Tian Shan orogen, that have been re-activated since ~ 12 Ma (e.g. Käßner et al. 2016; Abdulhameed et al. 2020), most

recently yielded during the Sary-Tash (*C*) and Karamyk (*H*) earthquakes on both ends of the Alai Valley, where the MPTS interacts with the Tian Shan. This requires the activation of a basal detachment deeper than that of the MPTS in Jurassic evaporites, that governs the fold-thrust belt of the Tajik Depression (e.g. Bekker 1996; Gagała et al. 2020). About E–W extension in the eastern Pamir along the Kongur Shan-Taxkorgan Normal Fault System (*I*), with northward increasing amounts (Robinson et al. 2007), is transferred into dextral strike-slip along the Muji Fault, and—under increasingly transpressional deformation—via the western Muji Fault and the Kyzylart Transfer Zone into and across the MPTS to the Pamir Frontal Thrust; the latter is characterized by range-front segmentation in thrusts and dextral strike-slip faults (e.g. Arrowsmith & Strecker 1999; Sippl et al. 2014).

The Pamir Plateau is dissected by the SKFS into the relative aseismic eastern Pamir block and the western Pamir with higher seismic activity (Schurr et al. 2014). Although we concur with the interpretation that the SKFS is part of the broad and distributed zone of sinistral strike-slip faulting along the western margin of the Indian mantle lithosphere indenter (Metzger et al. 2017), several aspects of this fault zone are particular: (1) The two largest historical crustal earthquakes of the Pamir interior—the 1911 and 2015 Sarez earthquakes—occurred at the southern end of the SKFS, approximately above the northeastern tip of the indenter (Fig. 1b); (2) the SKFS is morphologically well-expressed along the Sarez, Kokujbel, and Karakul segments, but loses expression entering the MPTS and the southwestern Pamir; (3) neotectonically, the northern Kokujbel and Karakul segments show the clearest evidence of \sim E–W extension, suggesting a northward increasing extensional component (from the Sarez to the Karakul segments), akin to that of the Kongur-Shan-Taxkorgan Normal Fault System. We speculate that the SKFS nucleated above the tip of the indenter and has been growing towards the NE and SW. The northward-increasing transtensional component in the Sarez aftershocks, the rift appearance of the Karakul segment, the anticlockwise change in strike of the northernmost SKFS segments, and the (little-studied) merger of these strands with the MPTS (Figs. 1b and 4) suggest increasingly stronger westward motion of material from the eastern Pamir in the east to the Tajik Depression to the west, and from the Hindu Kush and Karakorum in the south to the front of the Pamir in the north; this is traced by the GNSS velocity

vectors (Figure 1b; Metzger et al. 2020) and the anticlockwise rotations recorded in the northern Tajik Depression by paleomagnetic data (Pozzi & Feinberg 1991; Thomas et al. 1994). The SKFS at and south of Lake Sarez and the dextral Aksu-Murghab Fault Zone and its western prolongation, the Sarez-Murghab Thrust System, may outline—on first-order—the triangular shape of the tip of the mantle indenter by distributed deformation in the crust (Figs. 1 and 3).

While the eastern Pamir is growing outward into the Tarim basin by thrusting (F), the entire western Pamir has a significant component of \sim E-W extension (D), reflecting its collapse into the Tajik Depression. The westward increasing extensional component is accommodated by an increase in the dextral strike-slip component along the western MPTS (e.g., the Vakhsh Thrust System; Fig. 1b; Metzger et al. 2020), and the involvement of the southern Tian Shan in the Pamir deformation field by thrusting and dextral strike-slip faulting (H ; for the neotectonic evolution see Käßner et al. 2016).

Elliott et al. (2020) proposed that the fault zone on which the Khorog earthquake G^* is located as the source of the 1911 Sarez earthquake. The relative seismic quiescence between the Sarez aftershock B^* and the Khorog earthquake G^* (Figs. 2a, 3, and S8a) may suggest that the \sim 55 km long fault segment in between was not critically stressed, perhaps due to the occurrence of the 1911 earthquake on the enclosed segment. This length estimate would result in an empirical magnitude of $M7.0$ (Wells & Coppersmith 1994), which is in approximate agreement with the reported teleseismic body wave magnitude $m_b = 7.3 \pm 0.2$ of the 1911 earthquake (Kulikova et al. 2016).

6 FAULT INTERACTION

We argued at the outset that the probability of the three largest earthquakes occurring by chance in such close vicinity in space and time is low. In the present case, transferred stresses acted highly oblique or opposed to the slip directions of the receiving faults (Fig. 7). In the following, we investigate potential aseismic creep using geodetic time series and test if static Coulomb failure stress changes (Δ CFS) from the consecutive earthquake ruptures are able to explain rupture triggering of the neighboring faults.

6.1 Methods

6.1.1 InSAR Displacement and Fault Creep Model

To investigate the contribution of possible postseismic slip on the SKFS to the regional stress budget, we analyzed automatically generated radar interferograms (Lazecký et al. 2020) of ascending frame 100A_052 and descending frame 005D_050 (following Comet LiCS naming convention), covering the southern and northern part of the SKFS, respectively. We included all available data following the Sarez mainshock, that is 27 months for the southern frame (36 radar scenes, 93 interferograms; Fig. S10), and 5 months for the northern frame (5 radar scenes, 7 interferograms, Fig. S11), before they were affected by the Sary-Tash earthquake. After a visual data inspection and manual unwrapping error correction we calculated linear displacement rates using the small-baseline time-series analysis software *LiCSBAS* (Morishita et al. 2020). We subsampled (multi-looked) the original interferograms four times to a spatial resolution of ~ 400 m, clipped them to the area of interest and subtracted the predicted atmospheric signal delay using state-of-the-art weather models (Yu et al. 2018). We applied a temporal low-pass filter of 42 days and a spatial low-pass filter of 2 km to the time-series of frame 100A_052, and no filter to frame 005D_050 (Hooper 2008). Then we extracted linear rate maps (Fig. S12).

We converted the rate maps into displacement accumulated over the 202 days between the Sarez and Sary-Tash mainshocks, assuming a constant displacement rate due to post-seismic slip within the first few months following the Sarez main shock. We modeled the observed surface displacements using vertical, rectangular dislocation sources (Okada 1985) with uniform sinistral slip, assuming a homogeneous half space subsurface model with Lamé's parameters $\lambda = 32$ GPa and $G = 32$ GPa. Source location, depth and amount of slip were modified interactively using *kite* (Isken et al. 2017) until the predicted surface displacements fitted our observations reasonably well.

6.1.2 Coulomb Stress Changes

We modeled to which extent the stresses induced by the large earthquakes and corresponding foreshocks loaded or unloaded nearby fault segments by computing the change in Coulomb failure stress ΔCFS (Harris 1998):

$$\Delta CFS = \Delta\tau + \mu(\Delta\sigma_n + \Delta p). \quad (5)$$

$\Delta\tau$ is the change in shear stress on the fault (positive in slip direction), and $\Delta\sigma_n$ is the change in normal stress (a positive ΔCFS acts destabilizing). For most rocks μ is between 0.6 and 0.8 (Harris 1998). Under the assumption of undrained conditions (pore fluids do not escape or enter the fault), Δp is proportional to the mean stress change inside the fault (Rice & Cleary 1976):

$$\Delta p = -\beta \frac{\Delta\sigma_{kk}}{3}, \quad (6)$$

where $\Delta\sigma_{kk}$ is the sum of the diagonal elements of the stress tensor and β is the Skempton coefficient. β lies between 0.5 and 1.0 for rocks, but is typically between 0.7 and 0.9 (Cocco & Rice 2002; Harris 1998). β and μ are often combined into the apparent friction coefficient:

$$\mu' = \mu(1 - \beta). \quad (7)$$

We modeled the stress changes in response to the largest earthquakes, foreshocks and post-seismic slip transients using *pscmp* (Wang et al. 2006). We constructed dislocation sources (Okada 1985) from published fault-slip models (Metzger et al. 2017; He et al. 2018; Bie et al. 2018) and our own earthquake moment tensors. The fault length l and width w of moment tensor sources were estimated from M_W using the empirical scaling relationships of Wells & Coppersmith (1994):

$$l = 10^{(M_W - 4.38)/1.49}. \quad (8)$$

$$w = 10^{(M_W - 4.06)/2.25} \quad (9)$$

Slip s was calculated from $M_0 = AGs$, with the seismic moment M_0 , fault area A , and shear modulus $G = 32$ GPa. The slip sense was determined after resolution of the nodal plane ambiguity (Section 4). We then computed ΔCFS according to Eqs. (5) and (6) at the origin times and on the fault planes of the three large earthquakes and significant foreshocks. We used an elastic half space subsurface model with Lamé's parameters $\lambda = 32$ GPa and $G = 32$ GPa and chose $\mu = 0.8$ and

$\beta = 0.75$, so that the earthquake hypocenters received the largest ΔCFS concentration while the parameters remained in the physically plausible range. We tested $\mu = 0.4$ and $\beta = 0.5$ as well as the debated assumption that $\Delta p = 0$ (Harris 1998) by letting $\beta = 0$ and $\mu = \mu' = 0.2$ (Figs. S13 and S14). We found uncertainties in ΔCFS by randomly perturbing the modeling parameters using a normal distribution. The half space parameters λ and G were varied with a standard deviation of 5 GPa; the fault properties μ and β with one of 0.2 (assuring they remained in the $[0, 1]$ range); and the fault's strike, dip, and rake with one of 5° . We report the median, and the 5% and 95% quantiles of the resulting distributions (Tab. 1, Fig. S15 and S16).

6.2 Postseismic Creep on the Sarez-Karakul Fault System

The accumulated InSAR line-of-sight displacements between the Sarez and the Sary-Tash mainshocks show a distinct change along the mapped SKFS (Fig. 8a). While the data base of the southern frame is dense enough to provide a good signal-to-noise ratio in the time-series for detecting tectonic signals, the resulting rates in the northern frame—based on 5 radar scenes—may be dominated by local atmospheric conditions (Fig. S12).

The southern frame highlights sinistral motion and uplift east of the SKFS of ~ 8 mm in the look direction between the first satellite pass on December 30, 2015 and the Sary-Tash earthquake (Fig. 8a; Jin et al. 2022). The sinistral motion agrees with the co-seismic slip model of Metzger et al. (2017); the displacement amplitude is reasonable as well ($\sim 1\%$ of the co-seismic slip; Metzger et al. 2017), given that our observations do not capture the first three weeks of the post-seismic slip history.

In the northern frame, earthquake focal mechanisms indicate sinistral slip along the SKFS-segments north of Lake Karakul (Fig. 4a; see also Schurr et al. 2014). Even though the view direction is nearly insensitive to lateral slip, we assume—due to the significant across-strike displacement changes, the along-strike correlation of the signal, the seismic activity along the fault segments, and the location of events c' and C^* close to the northern tip of the SKFS—that the displacement signal is due to post-seismic creep on the SKFS; this allows to test whether creep may have contributed to the triggering of the Sary-Tash earthquake. The positive sign west of the

SKFS (the ground moved towards the satellite) indicates that the signal is not due to a normal faulting component.

We modeled our displacement observations as aseismic slip on seven vertical fault patches between 0.5 and 10.5 km depth along two segments of the SKFS between the epicenters of the Sarez and the Sary-Tash earthquakes (Kokujbel segment in the south, Karakul segment in the north; Figs. 4d and 8b). Our model indicates a maximum cumulative creep between 20 and 30 mm in the 202 days between the earthquakes on the Kokujbel segment ($\sim 35\text{--}55$ mm/yr, Fig. S12), which occupies part of the slip patch of the Sarez earthquake. On the Karakul segment, we find a total maximum displacement of 40 mm (~ 72 mm/yr) in the south to 25 mm (~ 45 mm/yr, Fig. S12) in the north. The segment links the co-seismically active part of the SKFS with the Kyzylart Transfer Zone, which connects the Muji Fault with the Pamir Frontal Thrust (Figs. 5a and 8a; Sippl et al. 2014).

6.3 Static Coulomb Stress Changes

The Sarez earthquake caused a long-wavelength positive ΔCFS on the Sary-Tash earthquake fault (Fig. 5g) with the highest values in the shallowest and westernmost part. It loaded the rupture plane, foreshock c' , and hypocenter C^* only weakly (~ 4 kPa; Tab. 1). Creep on the SKFS (Fig. 8) may have additionally loaded the Sary-Tash earthquake fault, mainly in the upper westernmost part, and with a lobe of increased ΔCFS that reaches towards the hypocenter at ~ 10 km depth (Fig. 5g). East of the hypocenter, the foreshock c' loaded the rim of the rupture plane. Together they caused a ΔCFS concentration of 4_{-3}^{+4} kPa at the hypocenter (Tab. 1; Fig. S15). Even with favorable (low- β) fault parameters, ΔCFS at the Sary-Tash hypocenter does not exceed 10 kPa (Fig. S13; see also Jin et al. 2022). These values may be just above the tidal shear stresses that the dip-slip fault experiences over the course of a day (~ 5 kPa; Tanaka et al. 2002). An additional ΔCFS contribution may be caused by viscous relaxation of the lower crust in the months following the Sarez earthquake, which would constitute an additional, deeper source with the same sense of motion and therefore a comparable effect as the earthquake itself. Static stress change induced by the 2008 Nura earthquake loaded the fault in the order of ~ 1 MPa (Fig. S13). Despite this

large stress perturbation, the Sary-Tash earthquake did not rupture before 2016. The area with the highest ΔCFS change west of the hypocenter did not rupture in an earthquake and did not produce many aftershocks (Fig. 5e-f). It might be that the MPTS in this part—close to the intersection with the SKFS—has a different orientation than modeled; ΔCFS may therefore be smaller or even negative. It is also possible that the MPTS was not critically stressed, for example because it ruptured in an earlier unrecorded earthquake. Lastly, the fault properties of the adjacent segment may be such that it slips aseismically.

The ΔCFS model for the Muji earthquake (Fig. 6d) suggests that the Sarez and Sary-Tash earthquakes unloaded the fault plane with a total negative ΔCFS of -19_{-6}^{+7} kPa (Figs. S14 and S16; Tab. 1). For the Sarez earthquake, the effect is mostly due to clamping of the Muji fault through normal stress and a slight loading opposite to the slip sense, i.e., relaxation. The Sary-Tash earthquake imposed sinistral strain on the Muji fault, as it pulled the northern wall towards the northwest relative to the southern wall; this is opposite to the dextral slip of the earthquake. The 2008 Nura earthquakes also imposed sinistral slip on the Muji fault. The foreshock *e'* stressed the hypocenter with $\Delta\text{CFS} \approx 60$ kPa. However, the remainder of the fault plane stayed in an unloaded and clamped state. As the foreshock had a focal mechanism and location almost identical to the mainshock, our model can neither explain triggering of the foreshock *e'* through CFS changes. We conclude that static stress changes counteracted the pending Muji rupture occurred due to another trigger.

Static stress changes are a viable trigger for the moderate earthquakes in the southern (e.g., events *B**, *G**, Tab. 1) and northern continuation of the SKFS (e.g., events 2, 4, 28; Tab. 1; Fig. 3), as well as all aftershocks of the Sary-Tash and Muji earthquakes (sequences *C* and *E* in Tab. 1). Our model indicates positive ΔCFS , typically between 10s and 100s kPa for these events. Similar stress magnitudes have been found for the aftershocks in the near-field (within about one rupture length) of many large earthquakes (Parsons & Dreger 2000; Toda et al. 1998; Sippl et al. 2014; Stein 1999; Wiseman & Burgmann 2011). We consider negative ΔCFS values artifacts of the too coarse fault-slip models that lack small scale slip heterogeneities. Earthquakes located at large

distances from any large earthquakes (>100 km; F^* , H^* , I^*) received no more than a miniscule Δ CFS and may have occurred independently of the large mainshocks.

6.4 Discussion of Fault Interaction

The characteristics of the 2015–2017 Pamir earthquake sequence differ from the sequences in the central Apennines (e.g., Chiaraluce et al. 2017), Baluchistan (Yadav et al. 2012), southern California (e.g., Hauksson et al. 1993; Parsons & Dreger 2000) and South Iceland (e.g., Hreinsdóttir et al. 2009) in that in the Pamir, faults interacted over much larger distances (≥ 100 km, compared to ≤ 30 km) and on kinematically dissimilar faults. In terms of duration, the sequences in Baluchistan and South Iceland came to rest within only a few months (Árnadóttir et al. 2003; Hreinsdóttir et al. 2009; Yadav et al. 2012), whereas the Sunda Arc (e.g., Wiseman & Burgmann 2011) and Southern California (e.g. Parsons & Dreger 2000) experienced recurring seismic activity within 7 years, and the southern Apennines within almost 10 years (e.g. Chiaraluce et al. 2017). The three $M_W > 6.4$ earthquakes of the present sequence occurred within a year and no $M_W > 5.5$ in the 5 years after.

The Sary-Tash earthquake—that motivated this study—and its foreshock c' , may have received a Δ CFS as low as 4 kPa, even if postseismic slip on the SKFS is considered. In case of the Muji earthquake, negative Δ CFS values indicate stabilization of the rupture plane and foreshock e' hypocenter, which suggests that it ruptured *despite of*—not due to—the static stress changes imposed by the previous earthquakes. We cannot exclude that the complexity of the Sary-Tash earthquake, indicated by the diverse aftershock mechanisms, may have caused a more complex deformation pattern below the MPTS, but we consider it unlikely that it reversed the modeled stress relaxation. The consistency between the large earthquake moment tensors and the regional stress tensor (Fig. 3) implies that the earthquakes responded to the long-term tectonic loading. That foreshock activity is at most weakly dependent on previous mainshock occurrence (Fig. 2) corroborates the inference that the static stress changes contributed only little to the total stress budget of the faults.

Low (~ 10 kPa) or negative Δ CFS values are regularly reported for subsequent earthquakes in a sequence (e.g. DeVries et al. 2018; Perfettini et al. 1999; Parsons & Dreger 2000; Ziv & Rubin

2000; Hardebeck et al. 1998; Wiseman & Burgmann 2011). Discrepancies between stress transfer models and actual earthquake occurrence could in some cases be ascribed to insufficient account for historic earthquakes (Mildon et al. 2017, 2019) or the predominant contribution of secular tectonic loading to earthquake occurrence (Mildon et al. 2017; Toda et al. 1998). To reconcile the timing of aftershocks, deliberately adjusted rate- and state-dependent fault friction parameters may be required (Dieterich 1994), which implies accelerating pre-slip on the fault (Dieterich 1992). In the present sequence, foreshocks indeed do show a tendency to surround the future rupture plane and approach the future hypocenter (Ellsworth & Bulut 2018; Schurr et al. 2020), but foreshock rate barely exceeded background rate (Schurr et al. 2014; Sippl et al. 2013b) and was not accelerating on any fault (Fig. 2c). Viscous processes have been suggested for the delayed triggering of the 1999 Hector Mine by the 1992 Landers earthquake (Hauksson et al. 1993). Postseismic models of the Sarez earthquake, however, suggest that visco-elastic relaxation can be neglected (Jin et al. 2022). Beyond the near-field, dynamic stress changes probably play an important role to generate aftershocks (Felzer & Brodsky 2006) or even trigger remote earthquakes (Gomberg & Johnson 2005). But dynamic stresses act almost immediately and do not provide an explanation for the multi-month delays between the events.

7 FLUID PROCESSES

That the observed seismicity, i.e., the three major sequences but also the moderate ones, to occur at with time increasing distances from the Sarez earthquake rupture that mimic a diffusion law (Fig. 2e, Eq. 3, Video S1), may point at a contribution of fluid migration to the earthquake triggering. Pore pressure counteracts normal stress and has a decisive effect on the frictional stability of faults. Faults are hydrological systems that store fluids if sealed and guide them if permeable. In sealed fault systems, fluids may be pressurized. An earthquake may breach seals and mobilize fluids (Sibson 1992). Brittle damage generated by main- and aftershocks can increase the permeability of a fault zone by orders of magnitude (Kitagawa et al. 2002; Miller & Nur 2000), particularly in the damage zone surrounding the fault core, creating pathways for fluids (Miller 2020). There is geophysical evidence for fluids in Pamir's upper crust that contains the fault systems

discussed here: a magneto-telluric profile—traversing the Pamir near the Sary-Tash earthquake—showed high-conductivity regions across the MPTS that were interpreted as due to aqueous fluids within the damage zones (Sass et al. 2014). This is corroborated by significantly increased P- to S-wave velocity ratios in the upper ~ 10 km of the crust along the MPTS detected by tomography (Sippl et al. 2013a). A contribution of poro-elastic rebound is consistent with the post-seismic deformation pattern of the Sarez earthquake (Jin et al. 2022). The fault zones that ruptured during the three major earthquakes are almost adjoining and likely interconnected. We hypothesize that fluids captured in the fault zone of the Sarez earthquake were co-seismically freed and pressured along the SKFS, where permeability may have been increased by brittle fracturing and transient stress changes (Fitzenz & Miller 2001; Manga et al. 2012), generating relatively distant and delayed aftershocks, reaching the MPTS and triggering the Sary-Tash earthquake. This may have initiated another fluid pressure wave sweeping through the fracture mesh connecting the MPTS and the Muji fault zone, eventually triggering the third event. Fluid triggering of the Muji earthquake may also account for the near-simultaneous rupture of both slip patches (Bie et al. 2018). The progression of a fluid front with time may be described by the square-root envelope-function of Eq. 3. Seismic event clouds that expand according to such a relationship are regularly observed in controlled fluid injection scenarios, such as hydrologically fracturing geothermal reservoirs (Ogwari & Horton 2016; Shapiro et al. 2003). For seismicity north of the Sarez earthquake, the hydraulic diffusivity D can be estimated between 30 and 40 m^2/s ; south of the earthquake between 12 and 20 m^2/s (Fig. 2e). Our estimates are stable with respect to the choice in origin (Fig. S8). Setting a new origin at the eastern end of the Sary-Tash earthquake for the later sweep to the Muji earthquake results in the same values. $D \approx 12\text{--}40 \text{ m}^2/\text{s}$ is well within the range suggested by Shapiro et al. (2003) of 10^{-2} to $10^{-1} \text{ m}^2/\text{s}$ for crystalline rocks to $10^2 \text{ m}^2/\text{s}$ for a recently ruptured subduction megathrust fault.

8 CONCLUSION

We analysed the seismic record of the earthquake sequence that struck the Pamir highlands in 2015–2017. Our observation started ~ 4 months before the initial $M_W 7.2$ Sarez earthquake, for

which no significant precursory seismic activity could be detected. The subsequent M_W 6.4 Sary-Tash and M_W 6.6 Muji earthquakes on adjacent faults, but more than 80 km away, showed foreshock activity, as did other M_W 4.4–5.7 earthquakes in the region. The aftershock seismicity traced the activated fault zones and testifies to the Pamir Plateau dissecting nature of the Sarez Karakul Fault System, interaction of the Main Pamir Thrust System with the northerly adjacent Tian Shan, and growth of the Pamir over the Tarim Basin in the east. The 1911 Sarez earthquake likely occurred on the fault segment enclosed by the M_W 5.3 Sarez aftershock and the M_W 4.9 Khorog earthquakes. Static stress transfer from the mainshocks, postseismic deformation and moderate foreshocks contributed at most subordinately to the stress budget of the activated fault segments. More likely, fluids migrated through the damaged fault zones and triggered the subsequent earthquakes. An improved detection and quantification of such fluid processes is required to gain a better understanding of the mechanisms that trigger seismicity during periods of seismic unrest.

ACKNOWLEDGMENTS

We thank the drivers and field participants from the Institute of Tibetan Plateau Research, especially Hongbing Liu, who helped to organize the station deployment; Christian Sippl, Sebastian Hainzl, and Rongjiang Wang for sharing code and discussion; Serge A. Shapiro for discussion; Chris Chafe for introducing data sonification; Ayleen Gaete for assisting the data processing. Funded by the CaTeNA project of the German Federal Ministry of Science and Education (support codes 03G0878A and 03G0878B) and German Research Council project RA 442/41. Open Access facilitated through project DEAL. Seismic data were handled using *obspy* (Krischer et al. 2015) and *pyrocko* (Heimann et al. 2017). Figures were created with the help of the *Generic Mapping Tools* (Wessel et al. 2013), *matplotlib* (Hunter 2007) and *Scientific Color Maps* (Crameri et al. 2020). Part of the instruments were provided by GIPP of GFZ Potsdam.

Data Availability

Seismic data are archived in the GEOFON data center (Yuan et al. 2018a,b). The seismic event and moment tensor catalogs are available through GFZ data services (Bloch et al. 2022). InSAR data

was downloaded from LiCSAR (Looking into the Continents from Space), which contains modified Copernicus Sentinel data analyzed by the Centre for the Observation and Modelling of Earthquakes, Volcanoes and Tectonics (COMET; <https://comet.nerc.ac.uk/comet-lics-portal>). LiCSAR uses JASMIN, the UK's collaborative data analysis environment.

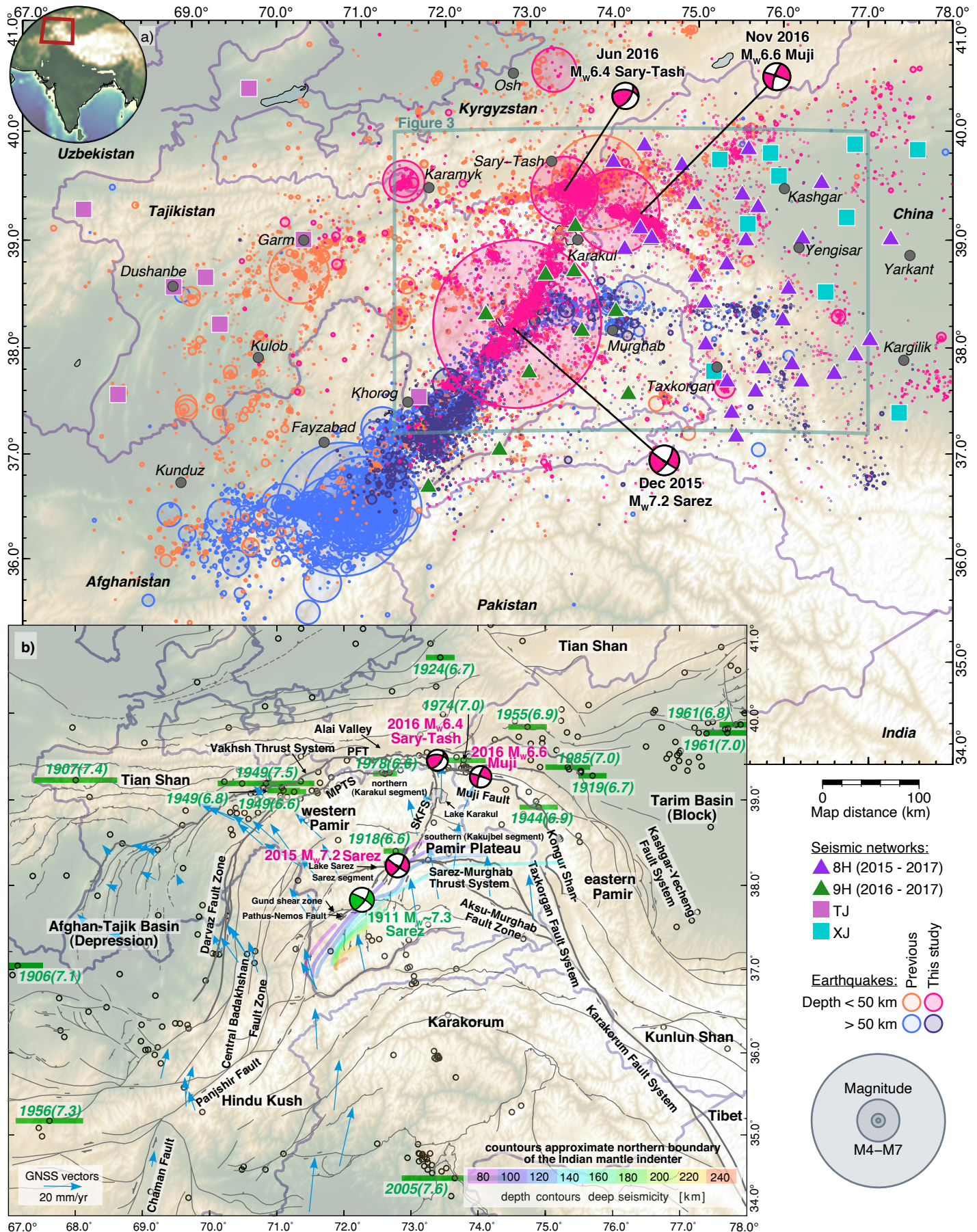


Figure 1. (a) Location of the study area, seismic stations, seismicity from this and previous (Schurr et al. 2014; Kufner et al. 2017, 2018) studies, and moment tensors of the three largest earthquakes of the sequence. Crustal seismicity (depth < 50 km) delineates the active fault zones. Intermediate depth seismicity (depth > 50 km) indicates subduction of Indian lithosphere beneath the Hindu Kush (Kufner et al. 2017, 2021) and delamination of Asian lithosphere beneath the Pamir (Sippl et al. 2013b; Bloch et al. 2021). (b) Cenozoic fault map with the neotectonic faults discussed in the text highlighted and named. Instrumentally recorded earthquakes since 1900 with $M > 5.5$ as black circles and $M > 6.5$ as green bars (Bondár et al. 2015; Di Giacomo et al. 2018; ISC 2021) indicating approximate rupture length (Wells & Coppersmith 1994). Focal mechanism of the 1911 Sarez earthquake is from Kulikova et al. (2016) and its location follows Elliott et al. (2020). Depth contours of intermediate-depth seismicity are from Schurr et al. (2014). Global Navigation Satellite System (GNSS) displacement rates from the Pamir Plateau and its western foreland are from Perry et al. (2019). MPTS: Main Pamir Thrust System. PFT: Pamir Frontal Thrust. SKFS: Sarez-Karakul Fault System.

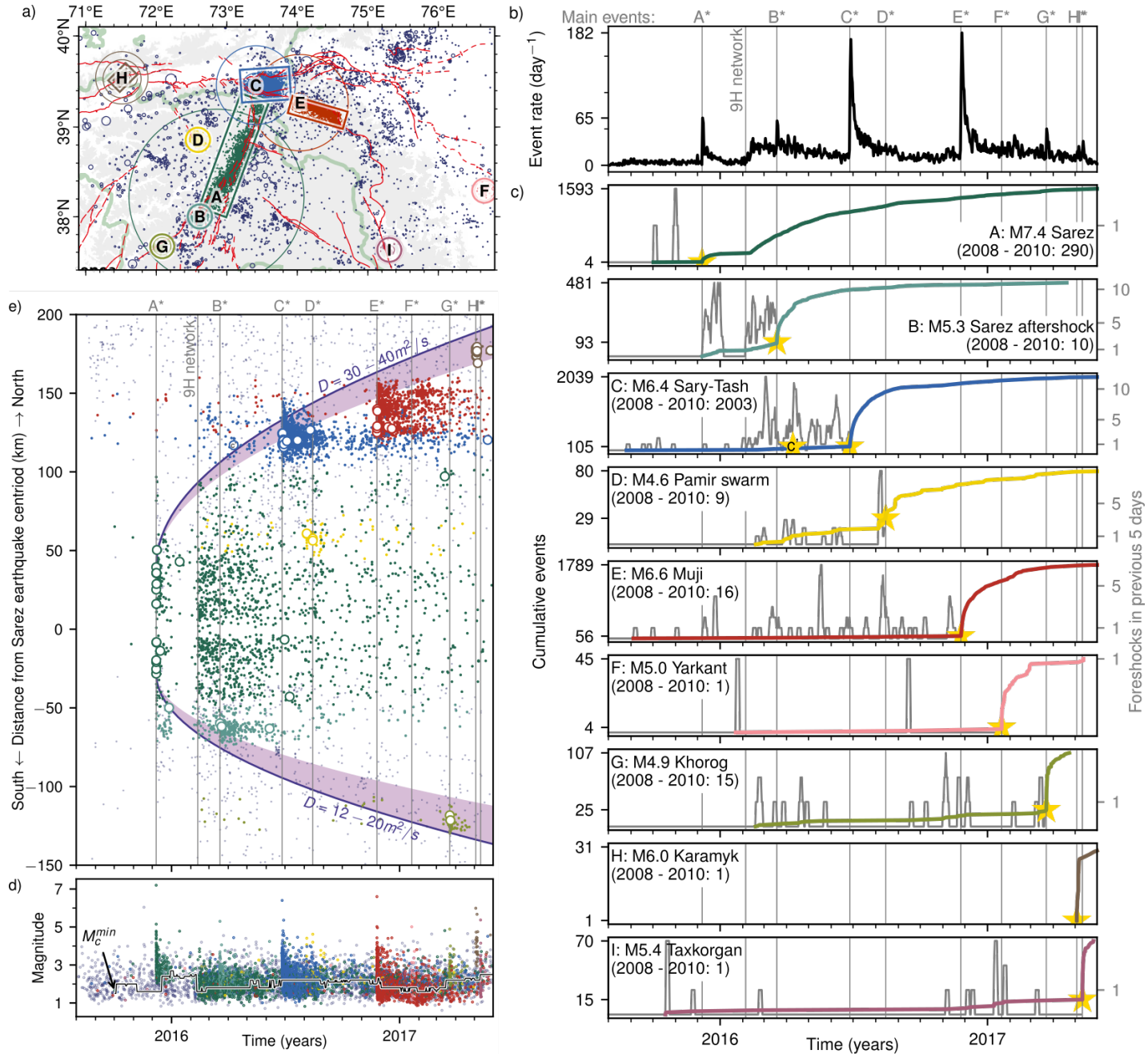


Figure 2. Spatio-temporal evolution of seismic activity. (a) Spatial definitions of sequences (A to I) with earthquakes color-coded as in the other subfigures and Fig. 3. See Video S1 for an animated and sonified version. (b) Seismic event rate over time. (c) Cumulative event number inside each sequence (colored) and 5-day moving window event number before the mainshock for each sequence (gray); event with largest magnitude in sequence is marked with a star and labeled on top. The number in the sequence of the strongest and the last event is labeled on the left. Cumulative event number from 2008 to 2010 for the specific region in parenthesis from Schurr et al. (2014). For aftershock event rate, see Fig. S9. (d) Magnitude over time with time variable minimum magnitude of completeness (M_c^{min}). (e) Spatio-temporal distribution of the seismic events with respect to the $M_W 7.2$ Sarez earthquake centroid. $M_W > 4$ events are highlighted as larger circles. The activation of the mainshock rupture planes mimics the diffusion equation 3 with scaling constant D (Figure S8). Most of the future mainshock volumes show foreshock activity, but foreshock activity is independent of mainshocks on other faults.

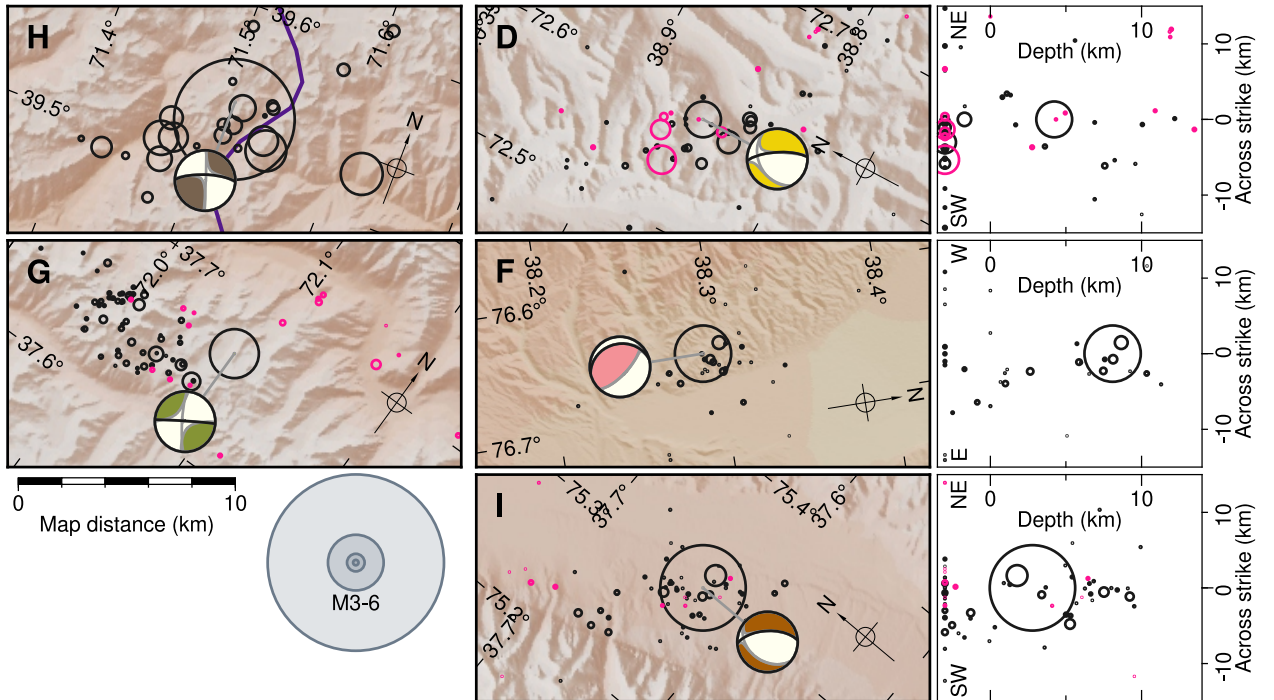
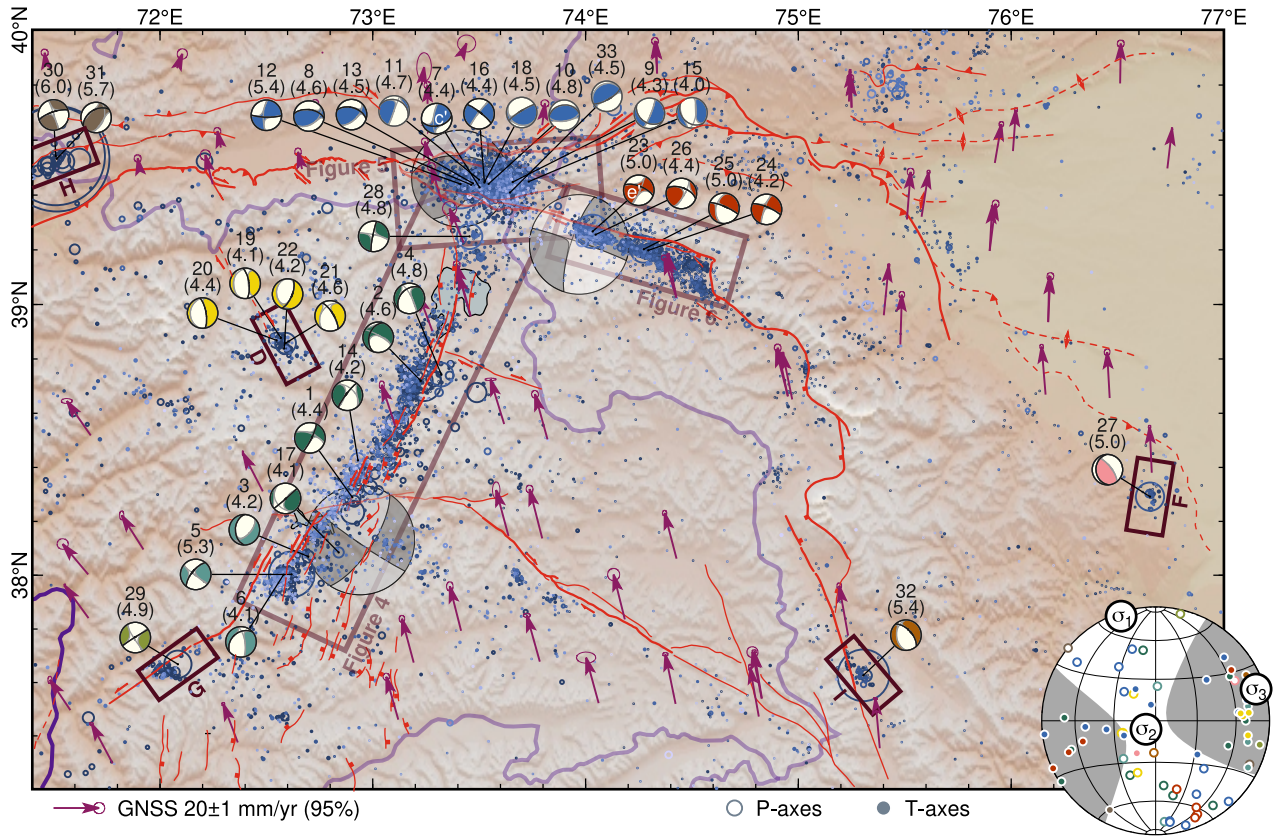


Figure 3. Summary of moment tensor results. Moment tensors colored by earthquake sequence as in Fig. 2 and numbered as in Tab. 1. M_W given in parenthesis. Interpreted fault planes are marked in the beach balls in black; fault planes preferred by stress inversion are marked in the beach balls in dark gray; auxiliary plane in light gray. Top: regional overview map. GNSS vectors from Zubovich et al. (2010) and Ischuk et al. (2013). Major neotectonic faults in red. Bottom: close-ups for sequences framed in the top subfigure; foreshocks (magenta); main- and aftershocks (black). (H, G) map views. (D, F, I) with additional across-strike profiles. Inset: stereographic projection of moment- and stress tensor principal axes. Positive areas of the stress tensor are shaded. Lower hemisphere stereographic projection.

Table 1. Source parameters and failure stresses of the large and moderate earthquakes for which a moment tensor is available. Strike, dip and rake of our preferred fault plane. # denotes our moment tensors shown in Figure 3; Sequence (Seq.) denotes the studied earthquake sequence, defined in Figure 2; * denotes the largest earthquake of the sequence. Depth is centroid depth, except for the three largest mainshocks, for which we report hypocentral depths. The change in Coulomb failure stress (Δ CFS) is due to all previous earthquakes. For c' and C*, Δ CFS without possible creep on the SKFS (Fig. 8) is given in brackets. Large negative Δ CFS in parenthesis are artifacts of the too coarse fault-slip models that lack small scale slip heterogeneities.

#	Seq.	Name	Time	M_W (°E)	Lon. (°N)	Lat. (km)	Depth (°)	Stike/Dip/Rake (kPa)	Δ CFS
	A*	Sarez	2015-12-07 07:50:04	7.2 ^a	72.853	38.223	0.9	214/83/8 ^a	0 ⁺⁰ ₋₀
1	A		2015-12-07 10:34:22	4.4	72.904	38.289	9.0	26/81/24	(-425 ⁺³⁴⁵ ₋₂₉₅)
2	A		2015-12-07 15:23:56	4.6	73.225	38.719	4.0	198/40/344	(-189 ⁺¹²² ₋₁₆₉)
3	B		2015-12-27 23:05:28	4.2	72.697	38.069	6.0	181/40/234	+27 ⁺⁵² ₋₃₄
4	A		2016-01-13 21:37:37	4.8	73.322	38.742	9.0	225/40/338	+102 ⁺⁶⁵ ₋₃₈
5	B*		2016-03-18 16:11:00	5.3	72.618	38.003	4.0	219/68/5	+132 ⁺⁷⁰ ₋₅₆
6	B		2016-03-21 05:32:27	4.1	72.581	38.002	4.0	230/38/325	(-306 ⁺¹²⁴ ₋₁₀₈)
7	c'		2016-04-09 16:19:33	4.4	73.502	39.428	9.0	79/50/157	+4 ⁺² ₋₂ [+8 ⁺³ ₋₃] ^d
	C*	Sary-Tash	2016-06-26 11:17:08	6.4 ^a	73.411	39.462	11.9	266/67/126 ^b	+4 ⁺⁴ ₋₃ [+3 ⁺⁴ ₋₅] ^d
8	C		2016-06-27 06:25:37	4.6	73.463	39.438	12.0	278/55/120	(-434 ⁺¹⁹⁸ ₋₂₇₀)
9	C		2016-06-27 07:34:13	4.3	73.657	39.447	6.0	123/37/194	+499 ⁺¹⁶⁰ ₋₁₃₈
10	C		2016-06-27 19:28:49	4.8	73.544	39.441	15.0	265/33/93	(-2007 ⁺⁵¹⁶ ₋₆₇₁)
11	C		2016-06-28 12:43:16	4.7	73.499	39.456	15.0	292/28/182	(-596 ⁺³⁵⁴ ₋₃₄₀)
12	C		2016-06-28 21:38:04	5.4	73.412	39.440	15.0	91/80/163	+111 ⁺²⁵¹ ₋₂₈₈
13	C		2016-06-29 08:08:14	4.5	73.471	39.443	12.0	287/52/139	(-791 ⁺²²⁵ ₋₂₄₉)
14	A		2016-06-30 07:09:43	4.2	72.930	38.426	18.0	217/82/320	(-1038 ⁺³⁴⁸ ₋₃₈₅)
15	C		2016-07-01 11:01:14	4.0	73.733	39.449	6.0	134/33/222	+335 ⁺⁹¹ ₋₁₁₀
16	C		2016-07-04 02:24:20	4.4	73.525	39.446	9.0	308/81/186	-9 ⁺⁹⁶ ₋₁₂₀
17	A		2016-07-08 12:10:25	4.1	72.840	38.085	4.0	49/88/306	(-82 ⁺²²¹ ₋₂₂₃)
18	C		2016-07-21 05:29:20	4.5	73.527	39.450	6.0	238/81/73	(-393 ⁺¹¹¹ ₋₁₂₅)
19	D		2016-08-04 21:34:41	4.1	72.568	38.877	4.0	352/69/263	+33 ⁺²⁰ ₋₁₄
20	D		2016-08-04 23:42:17	4.4	72.548	38.868	4.0	350/71/264	+10 ⁺¹⁸ ₋₁₈
21	D*		2016-08-14 15:05:20	4.6	72.590	38.858	6.0	329/72/234	+18 ⁺¹³ ₋₁₀
22	D		2016-08-14 15:11:39	4.2	72.584	38.838	4.0	22/66/287	+103 ⁺²⁴ ₋₂₆
23	e'		2016-11-25 14:18:59	5.0	74.034	39.267	15.0	291/68/173	-13 ⁺⁵ ₋₉
	E*	Muji	2016-11-25 14:24:27	6.6 ^a	74.039	39.269	13.7	106/88/184 ^c	+59 ⁺¹⁵⁷ ₋₁₇₂
24	E		2016-11-25 19:46:19	4.2	74.295	39.198	6.0	292/77/192	(-2072 ⁺⁷⁶² ₋₇₈₄)
25	E		2016-11-26 09:23:26	5.0	74.274	39.202	6.0	293/80/224	(-1175 ⁺⁵⁰¹ ₋₃₇₁)
26	E		2016-12-19 10:57:33	4.4	74.047	39.256	15.0	290/59/160	(-540 ⁺⁵²² ₋₃₆₃)
27	F*	Yarkant	2017-01-20 09:54:08	5.0	76.653	38.292	12.0	176/25/121	0 ⁺⁰ ₋₀
28	A		2017-03-14 11:07:11	4.8	73.455	39.249	12.0	191/84/351	+23 ⁺¹⁹ ₋₂₈
29	G*	Khorog	2017-03-22 11:27:02	4.9	72.084	37.668	12.0	238/88/8	+12 ⁺⁴ ₋₅
30	H*	Karamyk	2017-05-03 04:47:13	6.0	71.510	39.542	15.0	251/74/178	-3 ⁺¹ ₋₁
31	H		2017-05-05 05:09:35	5.7	71.514	39.532	12.0	237/48/115	(-1210 ⁺³¹⁸ ₋₄₃₀)
32	I*	Taxkorgan	2017-05-10 21:58:21	5.4	75.305	37.627	6.0	317/60/247	+0 ⁺⁰ ₋₀
33	C		2017-05-22 09:23:09	4.5	73.645	39.409	4.0	60/72/89	(-1356 ⁺³⁴⁸ ₋₃₆₁)

^aNEIC; ^bHe et al. (2018); ^cBie et al. (2018); ^d without creep (Fig. 8)

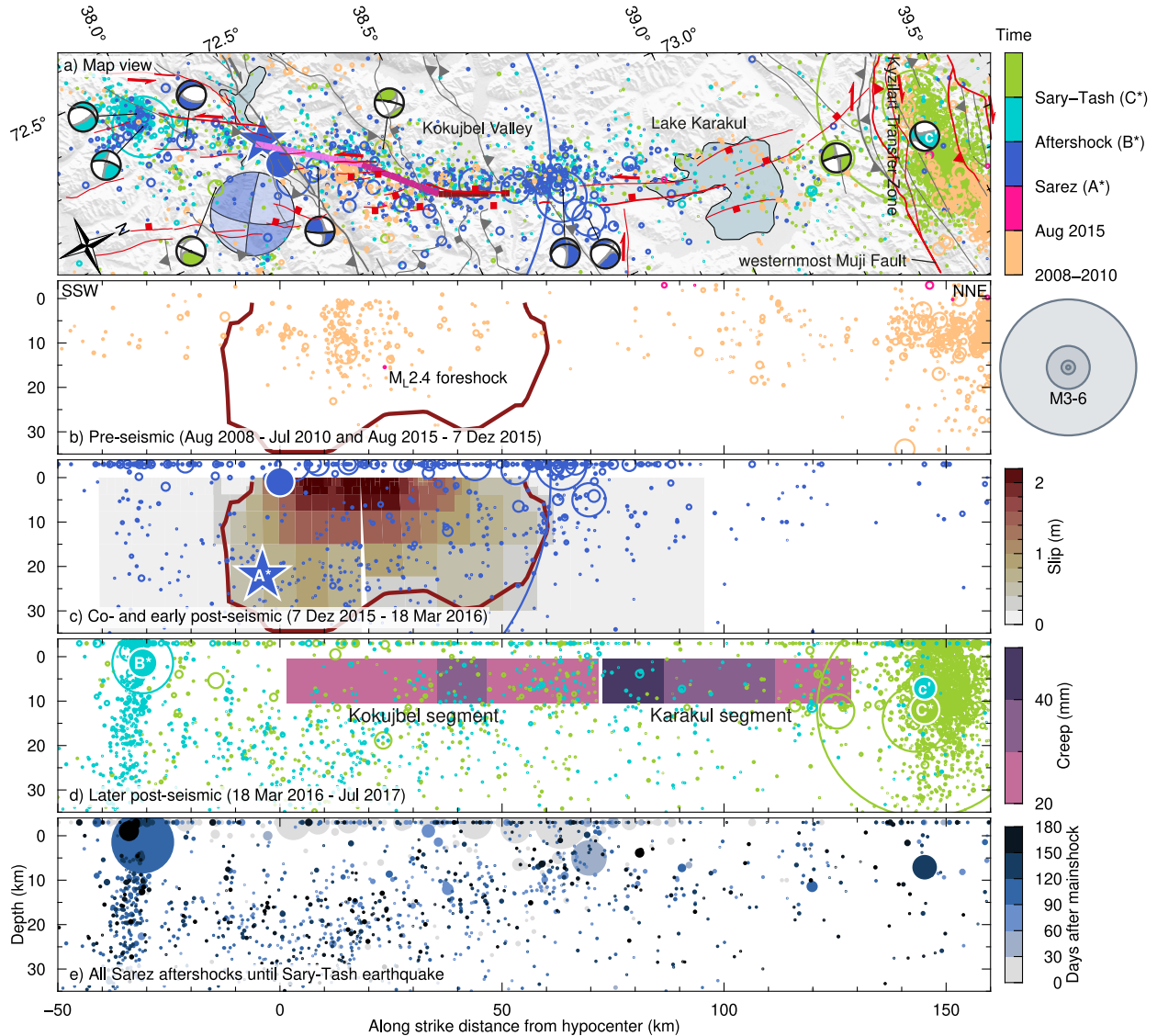


Figure 4. Time succession of seismicity and moment tensors of moderate earthquakes in the active part of the Sarez-Karakul Fault Zone; GEOFON focal mechanism of the mainshock (large beach ball); preferred hypocenter location by NEIC (star); 2008–2010 seismicity from Schurr et al. (2014). (a) Along-strike map view with the three segments of the co-seismic rupture highlighted (Metzger et al. 2017). Mapped Cenozoic structures in gray and neotectonic structures in red. Beach ball representation of moment tensors (Tab. 1) with preferred fault plane in black. (b–d) Along strike profiles. (b) Seismicity before the Sarez mainshock. 10% of maximum future slip contoured. (c) Early aftershock seismicity until aftershock B^* . Co-seismic slip from Metzger et al. (2017). (d) Later aftershock seismicity. Cumulative creep model as in Fig. 8 between A^* and C^* (Tab. 1). (e) Time succession of the Sarez aftershocks until the Sary-Tash earthquake. The larger ($M > 4$) earthquakes migrated away from the mainshock rupture. No significant immediate foreshock activity was detected for the Sarez earthquake. The rupture plane has been constantly active throughout 2008–2010. Aftershock seismicity skirts around the co-seismic slip patch.

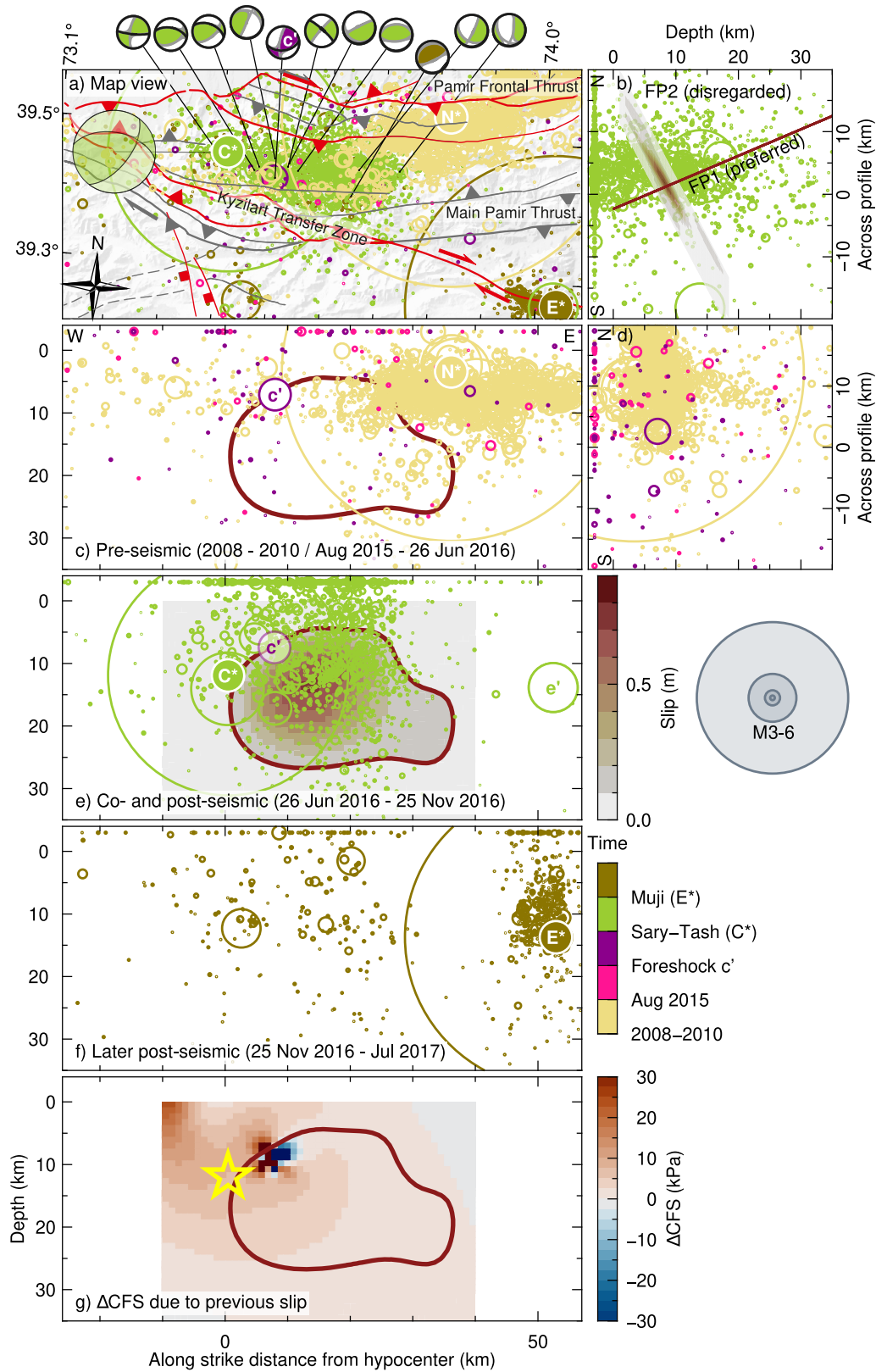


Figure 5. Time succession of seismicity and moment tensors of moderate earthquakes in the active part of the Main Pamir Thrust System; GEOFON focal mechanism of the mainshock (large beach ball); 2008–2010 seismicity from Schurr et al. (2014); hypocenter of the 2008 Nura earthquake (N^* ; Sippl et al. 2014) and fore- and mainshocks discussed in the text (c' , C^* , e' , E^*). (a) Along-strike map view. Mapped Cenozoic structures in gray and neotectonic structures in red. Beach ball representation of moment tensors (Tab. 1) with preferred fault plane in black. (b, d) Across-strike profiles. (c, e, f) Along-strike profiles. (b) Aftershock seismicity and the two possible fault planes of the mainshock (He et al. 2018). FP1 is preferred, because aftershock seismicity concentrates in the hanging wall. (c, d) Seismicity before the Sary-Tash mainshock; 10% of maximum future slip contoured. (e) Early aftershock seismicity until subsequent Muji mainshock E^* . Co-seismic slip from He et al. (2018). (f) Later aftershock seismicity and spatial configuration with the Muji earthquake (E^*). (g) Δ CFS on the fault plane. Star marks the hypocenter. Foreshock activity left out the future rupture area and grossly concentrated around the future hypocenter since c' . Note the lesser depth extent of the Nura aftershock seismicity.

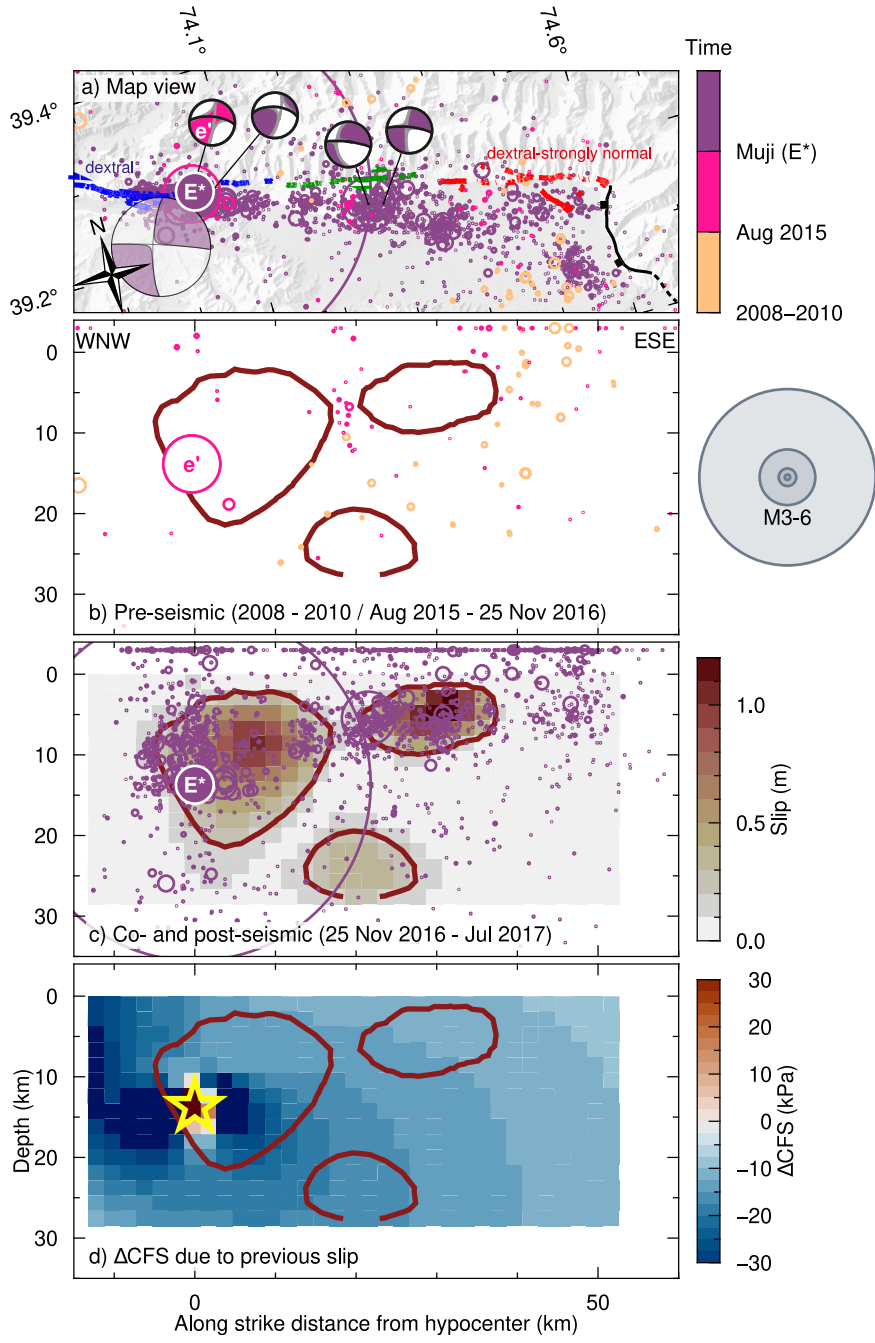


Figure 6. Time succession of seismicity and moment tensors of moderate earthquakes in the active part of the Muji Fault; GEOFON focal mechanism (large beach ball); 2008–2010 seismicity from Schurr et al. (2014); fore- and mainshock hypocenters (e' , E^*). (a) Along-strike map view. Beach ball representation of moment tensors (Tab. 1) with preferred fault plane in black. Surface traces (blue, green, red) of the Muji-Fault earthquake and other faults modified from Li et al. (2019) (b, c) Along-strike profiles. (b) Seismicity before the mainshock; 10% of maximum future slip contoured, the lowermost slip patch is not resolved. (c) Aftershock seismicity and co-seismic slip model (Bie et al. 2018). (d) Δ CFS model due to all previous earthquakes. Star: earthquake hypocenter. Foreshock activity left out the future rupture area. e' occurred 12 minutes before the mainshock, very close to the hypocenter location. Stress transfer from the previous earthquakes acted stabilizing on the fault plane.

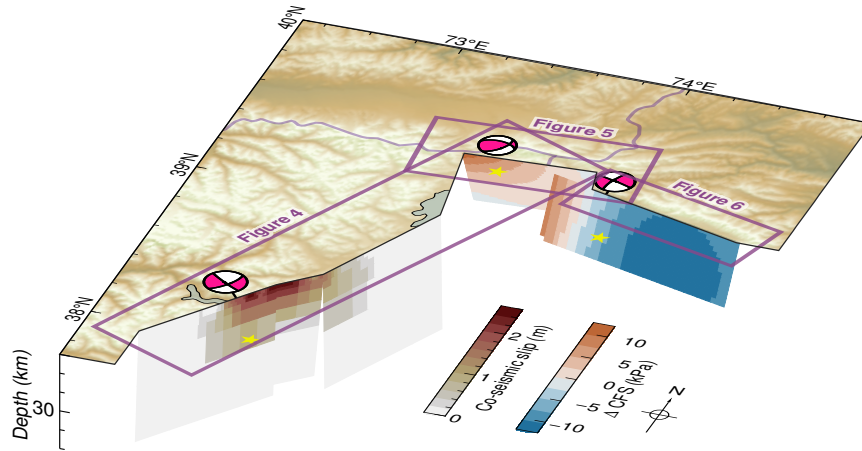


Figure 7. Perspective view onto the three activated fault segments, with slip of the Sarez earthquake (Fig. 4) and thereby imposed static change in Coulomb Failure Stress (ΔCFS) on the Sary-Tash (Fig. 5) and Muji (Fig. 6) earthquake faults. Stars: earthquake hypocenters. The Coulomb Failure Stress change on the fault planes of the future large earthquakes is small (~ 5 kPa) or even negative (~ -7 kPa).

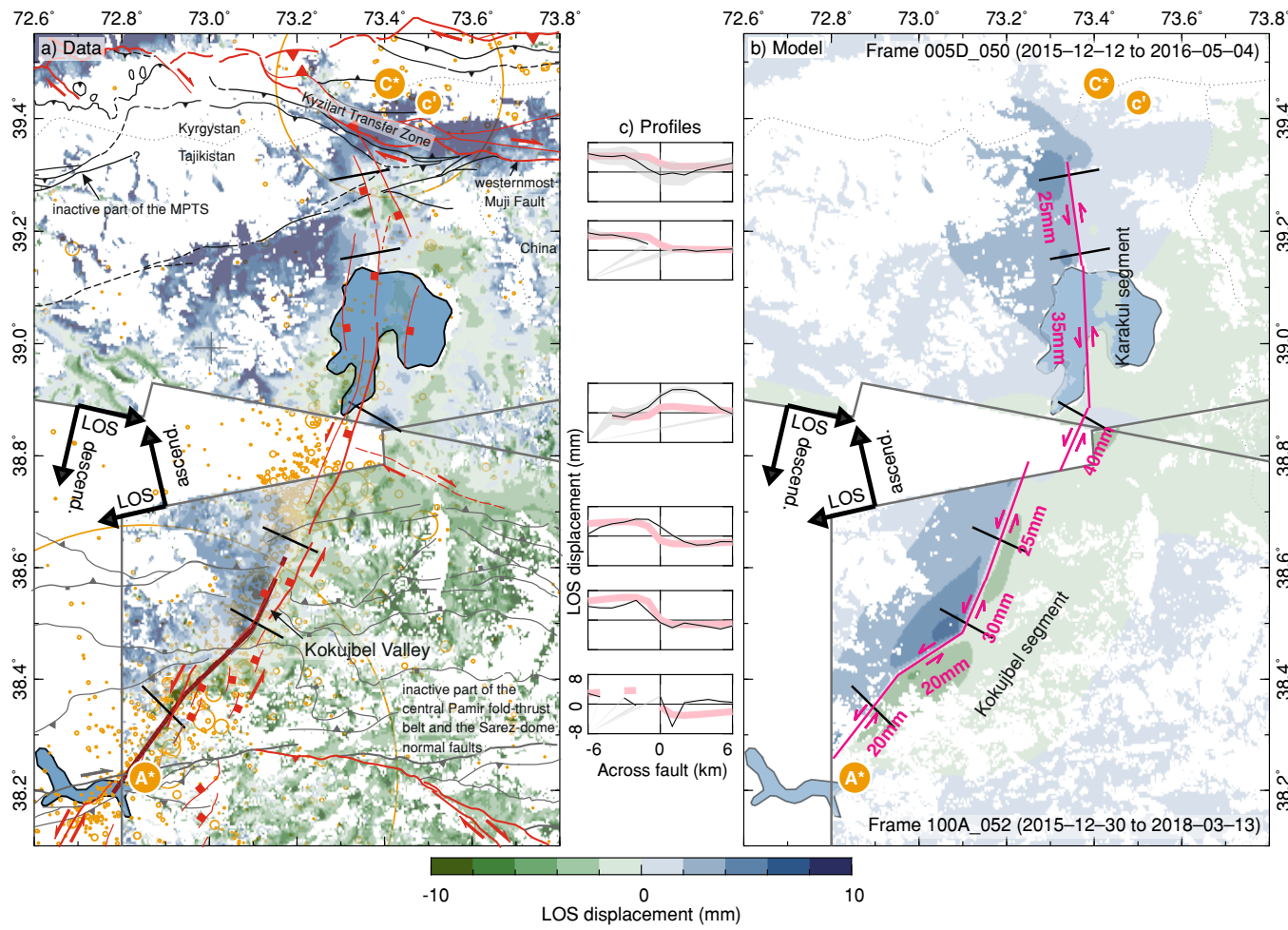


Figure 8. Post-seismic displacement on the Sarez-Karakul Fault System. (a) InSAR displacement map derived from the displacement-rate map (Fig. S12). Seismicity between A^* and C^* , main- and foreshock hypocenters highlighted in orange. Mapped Cenozoic structures in gray and neotectonic structures in red. (b) Fault creep model and synthetic data. (c) Across-strike displacement profiles with data (black), nominal data uncertainty (gray), and model (pink). Displacement is accumulated in 202 days between events A^* and C^* . LOS: line-of-sight vector. See Fig. 4d for along-strike view of the creep model and Fig. S12 for uncertainty in map view.

REFERENCES

- Abdulhameed, S., Ratschbacher, L., Jonckheere, R., Gagała, Ł., Enkelmann, E., Käbner, A., Kars, M. A., Szulc, A., Kufner, S.-K., Schurr, B., et al., 2020. Tajik basin and southwestern Tian Shan, northwestern India-Asia collision zone: 2. Timing of basin inversion, Tian Shan mountain building, and relation to Pamir-plateau advance and deep India-Asia indentation, *Tectonics*, **39**(5), e2019TC005873.
- Aldersons, F., 2004. *Toward three-dimensional crustal structure of the Dead Sea region from local earthquake tomography*, Ph.D. thesis, Tel-Aviv University.
- Árnadóttir, T., Jónsson, S., Pedersen, R., & Gudmundsson, G. B., 2003. Coulomb stress changes in the South Iceland Seismic Zone due to two large earthquakes in June 2000, *Geophysical Research Letters*, **30**(5), n/a–n/a.
- Arrowsmith, J. R. & Strecker, M., 1999. Seismotectonic range-front segmentation and mountain-belt growth in the Pamir-Alai region, Kyrgyzstan (India-Eurasia collision zone), *Geological Society of America Bulletin*, **111**(11), 1665–1683.
- Bekker, Y. A., 1996. Tectonics of the Afghan-Tajik depression, *Geotectonics*, **30**(1), 64–70.
- Bie, L., Hicks, S., Garth, T., Gonzalez, P., & Rietbrock, A., 2018. ‘Two go together’: Near-simultaneous moment release of two asperities during the 2016 Mw 6.6 Muji, China earthquake, *Earth and Planetary Science Letters*, **491**, 34–42.
- Bloch, W., Schurr, B., Yuan, X., Ratschbacher, L., Reuter, S., Kufner, S.-K., Xu, Q., & Zhao, J., 2021. Structure and stress field of the lithosphere between Pamir and Tarim, *Geophysical Research Letters*, **48**(22).
- Bloch, W., Schurr, B., Yuan, X., Xu, Q., Zhao, J., Murodkulov, S., & Oimuhammadzoda, I., 2022. Earthquake and moment tensor catalogs of the 2015–2017 Pamir earthquake sequence, *GFZ Data Services*.
- Bondár, I., Engdahl, E. R., Villaseñor, A., Harris, J., & Storchak, D., 2015. ISC-GEM: Global instrumental earthquake catalogue (1900–2009), II. location and seismicity patterns, *Physics of the Earth and Planetary Interiors*, **239**, 2–13.
- Bormann, P. & Dewey, J. W., 2012. The new IASPEI standards for determining magnitudes from digital data and their relation to classical magnitudes, in *New Manual of Seismological Observatory Practice 2 (NMSOP-2)*, pp. 1–44, Deutsches GeoForschungsZentrum GFZ.
- Bouchon, M., 1981. A simple method to calculate Green’s functions for elastic layered media, *Bulletin of the Seismological Society of America*, **71**(4), 959–971.
- Briggs, R. W., Sieh, K., Meltzner, A. J., Natawidjaja, D., Galetzka, J., Suwargadi, B., Hsu, Y., Simons, M., Hananto, N., Suprihanto, I., Prayudi, D., Avouac, J.-P., Prawirodirdjo, L., & Bock, Y., 2006. Deformation and slip along the Sunda megathrust in the great 2005 Nias-Simeulue earthquake, *Science*, **311**(5769), 1897–1901.
- Burtman, V. S. & Molnar, P. H., 1993. *Geological and geophysical evidence for deep subduction of*

- continental crust beneath the Pamir*, vol. 281, Geological Society of America.
- Chen, K., Avouac, J.-P., Aati, S., Milliner, C., Zheng, F., & Shi, C., 2020. Cascading and pulse-like ruptures during the 2019 Ridgecrest earthquakes in the Eastern California Shear Zone, *Nature communications*, **11**(1), 1–8.
- Chevalier, M.-L., Pan, J., Li, H., Liu, D., & Wang, M., 2015. Quantification of both normal and right-lateral late Quaternary activity along the Kongur Shan extensional system, Chinese Pamir, *Terra Nova*, **27**(5), 379–391.
- Chiaraluce, L., Ellsworth, W., Chiarabba, C., & Cocco, M., 2003. Imaging the complexity of an active normal fault system: The 1997 Colfiorito (central Italy) case study, *Journal of Geophysical Research: Solid Earth*, **108**(B6).
- Chiaraluce, L., Stefano, R. D., Tinti, E., Scognamiglio, L., Michele, M., Casarotti, E., Cattaneo, M., Gori, P. D., Chiarabba, C., Monachesi, G., Lombardi, A., Valoroso, L., Latorre, D., & Marzorati, S., 2017. The 2016 Central Italy seismic sequence: A first look at the mainshocks, aftershocks, and source models, *Seismological Research Letters*, **88**(3), 757–771.
- Cocco, M. & Rice, J. R., 2002. Pore pressure and poroelasticity effects in coulomb stress analysis of earthquake interactions, *Journal of Geophysical Research: Solid Earth*, **107**(B2), ESE 2–1–ESE 2–17.
- Comino, J. Á. L., Heimann, S., Cesca, S., Milkereit, C., Dahm, T., & Zang, A., 2017. Automated full waveform detection and location algorithm of acoustic emissions from hydraulic fracturing experiment, *Procedia engineering*, **191**, 697–702.
- Cowgill, E., 2009. Cenozoic right-slip faulting along the eastern margin of the Pamir salient, northwestern China, *Geological Society of America Bulletin*, **122**(1-2), 145–161.
- Crameri, F., Shephard, G. E., & Heron, P. J., 2020. The misuse of colour in science communication, *Nature communications*, **11**(1), 1–10.
- Das, S. & Henry, C., 2003. Spatial relation between main earthquake slip and its aftershock distribution, *Reviews of Geophysics*, **41**(3).
- DeVries, P. M. R., Viégas, F., Wattenberg, M., & Meade, B. J., 2018. Deep learning of aftershock patterns following large earthquakes, *Nature*, **560**(7720), 632–634.
- Di Giacomo, D., Engdahl, E. R., & Storchak, D. A., 2018. The ISC-GEM earthquake catalogue (1904–2014): status after the extension project, *Earth System Science Data*, **10**(4), 1877–1899.
- Diehl, T., Deichmann, N., Kissling, E., & Husen, S., 2009. Automatic S-wave picker for local earthquake tomography, *Bulletin of the Seismological Society of America*, **99**(3), 1906–1920.
- Dieterich, J. H., 1992. Earthquake nucleation on faults with rate-and state-dependent strength, *Tectonophysics*, **211**(1-4), 115–134.
- Dieterich, J. H., 1994. A constitutive law for rate of earthquake production and its application to earthquake clustering, *Journal of Geophysical Research: Solid Earth*, **99**(B2), 2601–2618.

- Einarsson, P., Björnsson, S., Foulger, G., Stefánsson, R., & Skaftadóttir, T., 1981. Seismicity pattern in the South Iceland Seismic Zone, in *Maurice Ewing Series*, pp. 141–151, American Geophysical Union.
- Elliott, A., Elliott, J., Hollingsworth, J., Kulikova, G., Parsons, B., & Walker, R., 2020. Satellite imaging of the 2015 M 7.2 earthquake in the Central Pamir, Tajikistan, elucidates a sequence of shallow strike-slip ruptures of the Sarez-Karakul fault, *Geophysical Journal International*, **221**(3), 1696–1718.
- Ellsworth, W. L. & Bulut, F., 2018. Nucleation of the 1999 Izmit earthquake by a triggered cascade of foreshocks, *Nature Geoscience*, **11**(7), 531–535.
- Ellsworth, W. L., Giardini, D., Townend, J., Ge, S., & Shimamoto, T., 2019. Triggering of the Pohang, Korea, earthquake (Mw 5.5) by enhanced geothermal system stimulation, *Seismological Research Letters*.
- Fan, G., Ni, J. F., & Wallace, T. C., 1994. Active tectonics of the Pamirs and Karakorum, *Journal of Geophysical Research: Solid Earth*, **99**(B4), 7131–7160.
- Felzer, K. R. & Brodsky, E. E., 2006. Decay of aftershock density with distance indicates triggering by dynamic stress, *Nature*, **441**(7094), 735–738.
- Fitzenz, D. D. & Miller, S. A., 2001. A forward model for earthquake generation on interacting faults including tectonics, fluids, and stress transfer, *Journal of Geophysical Research: Solid Earth*, **106**(B11), 26689–26706.
- Freed, A. M. & Lin, J., 2001. Delayed triggering of the 1999 Hector Mine earthquake by viscoelastic stress transfer, *Nature*, **411**(6834), 180–183.
- Gagała, Ł., Ratschbacher, L., Ringenbach, J.-C., Kufner, S.-K., Schurr, B., Dedow, R., Abdulhameed, S., Le Garzic, E., Gadoev, M., & Oimahmadov, I., 2020. Tajik Basin and Southwestern Tian Shan, Northwestern India-Asia Collision Zone: 1. Structure, Kinematics, and Salt Tectonics in the Tajik Fold-and-Thrust Belt of the Western Foreland of the Pamir, *Tectonics*, **39**(5), e2019TC005871.
- Gomberg, J. & Johnson, P., 2005. Dynamic triggering of earthquakes, *Nature*, **437**(7060), 830–830.
- Hamling, I. J. & Upton, P., 2018. Observations of aseismic slip driven by fluid pressure following the 2016 Kaikōura, New Zealand, earthquake, *Geophysical Research Letters*, **45**(20).
- Hardebeck, J. L., Nazareth, J. J., & Hauksson, E., 1998. The static stress change triggering model: Constraints from two southern California aftershock sequences, *Journal of Geophysical Research: Solid Earth*, **103**(B10), 24427–24437.
- Harris, R. A., 1998. Introduction to special section: Stress triggers, stress shadows, and implications for seismic hazard, *Journal of Geophysical Research: Solid Earth*, **103**(B10), 24347–24358.
- Hauksson, E., Jones, L. M., Hutton, K., & Eberhart-Phillips, D., 1993. The 1992 Landers earthquake sequence: Seismological observations, *Journal of Geophysical Research: Solid Earth*, **98**(B11), 19835–19858.
- He, P., Hetland, E. A., Niemi, N. A., Wang, Q., Wen, Y., & Ding, K., 2018. The 2016 Mw 6.5 Nura

- earthquake in the Trans Alai range, northern Pamir: possible rupture on a back-thrust fault constrained by Sentinel-1A radar interferometry, *Tectonophysics*, **749**, 62–71.
- Heimann, S., Kriegerowski, M., Isken, M., Cesca, S., Daout, S., Grigoli, F., Juretzek, C., Megies, T., Nooshiri, N., Steinberg, A., et al., 2017. Pyrocko - An open-source seismology toolbox and library, *GFZ Data Services*.
- Hooper, A., 2008. A multi-temporal InSAR method incorporating both persistent scatterer and small baseline approaches, *Geophysical Research Letters*, **35**(16).
- Hreinsdóttir, S., Árnadóttir, T., Decriem, J., Geirsson, H., Tryggvason, A., Bennett, R. A., & LaFemina, P., 2009. A complex earthquake sequence captured by the continuous GPS network in SW Iceland, *Geophysical Research Letters*, **36**(12).
- Hunter, J. D., 2007. Matplotlib: A 2D graphics environment, *Computing in Science & Engineering*, **9**(3), 90–95.
- ISC, 2021. ISC-GEM Earthquake Catalogue, Tech. rep., International Seismological Centre.
- Ischuk, A., Bendick, R., Rybin, A., Molnar, P., Khan, S. F., Kuzikov, S., Mohadjer, S., Saydullaev, U., Ilyasova, Z., Schelochkov, G., et al., 2013. Kinematics of the Pamir and Hindu Kush regions from GPS geodesy, *Journal of Geophysical Research: Solid Earth*, **118**(5), 2408–2416.
- Isken, M., Sudhaus, H., Heimann, S., Steinberg, A., Daout, S., & Vasyura-Bathke, H., 2017. Kite-software for rapid earthquake source optimisation from InSAR surface displacement, *GFZ Data Services*.
- Jade, S., Bhatt, B., Yang, Z., Bendick, R., Gaur, V., Molnar, P., Anand, M., & Kumar, D., 2004. GPS measurements from the Ladakh Himalaya, India: Preliminary tests of plate-like or continuous deformation in Tibet, *Geological Society of America Bulletin*, **116**(11-12), 1385–1391.
- Jin, Z., Fialko, Y., Zubovich, A., & Schöne, T., 2022. Lithospheric deformation due to the 2015 M7.2 Sarez (Pamir) earthquake constrained by 5 years of space geodetic observations, *Journal of Geophysical Research: Solid Earth*, **127**(4).
- Käßner, A., Ratschbacher, L., Jonckheere, R., Enkelmann, E., Khan, J., Sonntag, B.-L., Gloaguen, R., Gadoev, M., & Oimahmadov, I., 2016. Cenozoic intracontinental deformation and exhumation at the northwestern tip of the India-Asia collision—southwestern Tian Shan, Tajikistan, and Kyrgyzstan, *Tectonics*, **35**(9), 2171–2194.
- Kissling, E., Ellsworth, W., Eberhart-Phillips, D., & Kradolfer, U., 1994. Initial reference models in local earthquake tomography, *Journal of Geophysical Research: Solid Earth*, **99**(B10), 19635–19646.
- Kitagawa, Y., Fujimori, K., & Koizumi, N., 2002. Temporal change in permeability of the rock estimated from repeated water injection experiments near the Nojima fault in Awaji Island, Japan, *Geophysical research letters*, **29**(10), 121–1.
- Kreemer, C., Blewitt, G., & Klein, E. C., 2014. A geodetic plate motion and global strain rate model, *Geochemistry, Geophysics, Geosystems*, **15**(10), 3849–3889.

- Krischer, L., Megies, T., Barsch, R., Beyreuther, M., Lecocq, T., Caudron, C., & Wassermann, J., 2015. ObsPy: A bridge for seismology into the scientific Python ecosystem, *Computational Science & Discovery*, **8**(1), 014003.
- Kufner, S.-K., Schurr, B., Sippl, C., Yuan, X., Ratschbacher, L., Ischuk, A., Murodkulov, S., Schneider, F., Mechie, J., Tilmann, F., et al., 2016. Deep India meets deep Asia: Lithospheric indentation, delamination and break-off under Pamir and Hindu Kush (Central Asia), *Earth and Planetary Science Letters*, **435**, 171–184.
- Kufner, S.-K., Schurr, B., Haberland, C., Zhang, Y., Saul, J., Ischuk, A., & Oimahmadov, I., 2017. Zooming into the Hindu Kush slab break-off: A rare glimpse on the terminal stage of subduction, *Earth and Planetary Science Letters*, **461**, 127–140.
- Kufner, S.-K., Schurr, B., Ratschbacher, L., Murodkulov, S., Abdulhameed, S., Ischuk, A., Metzger, S., & Kakar, N., 2018. Seismotectonics of the Tajik basin and surrounding mountain ranges, *Tectonics*, **37**(8), 2404–2424.
- Kufner, S.-K., Kakar, N., Bezada, M., Bloch, W., Metzger, S., Yuan, X., Mechie, J., Ratschbacher, L., Murodkulov, S., Deng, Z., et al., 2021. The Hindu Kush slab break-off as revealed by deep structure and crustal deformation, *Nature communications*, **12**(1), 1–11.
- Kulikova, G., Schurr, B., Krüger, F., Brzoska, E., & Heimann, S., 2016. Source parameters of the Sarez-Pamir earthquake of 1911 February 18, *Geophysical Journal International*, **205**(2), 1086–1098.
- Langston, C. A. & Dermengian, J. M., 1981. Comment on ‘seismotectonic aspects of the Markansu Valley, Tadjikistan, earthquake of august 11, 1974’ by James Jackson, Peter Molnar, Howard Patton, and Thomas Fitch, *Journal of Geophysical Research: Solid Earth*, **86**(B2), 1091–1093.
- Lazecký, M., Spaans, K., González, P. J., Maghsoudi, Y., Morishita, Y., Albino, F., Elliott, J., Greenall, N., Hatton, E., Hooper, A., Juncu, D., McDougall, A., Walters, R. J., Watson, C. S., Weiss, J. R., & Wright, T. J., 2020. Licsar: An automatic insar tool for measuring and monitoring tectonic and volcanic activity, *Remote Sensing*, **12**(15).
- Lee, W. H. K. & Lahr, J. C., 1972. *HYP071: A computer program for determining hypocenter, magnitude, and first motion pattern of local earthquakes*, 75-311, US Department of the Interior, Geological Survey, National Center for determining hypocenter, magnitude, and first motion pattern of local earthquakes.
- Li, J., Liu, G., Qiao, X., Xiong, W., Wang, X., Liu, D., Sun, J., Yushan, A., Yusan, S., Fang, W., & Wang, Q., 2018. Rupture characteristics of the 25 November 2016 Aketao earthquake (mw 6.6) in eastern Pamir revealed by GPS and teleseismic data, *Pure and Applied Geophysics*, **175**(2), 573–585.
- Li, T., Schoenbohm, L. M., Chen, J., Yuan, Z., Feng, W., Li, W., Xu, J., Owen, L. A., Sobel, E. R., Zhang, B., et al., 2019. Cumulative and Coseismic (During the 2016 Mw 6.6 Aketao Earthquake) Deformation of the Dextral-Slip Muji Fault, Northeastern Pamir Orogen, *Tectonics*, **38**(11), 3975–3989.
- Lorenzo-Martín, F., Roth, F., & Wang, R., 2006. Elastic and inelastic triggering of earthquakes in the

- North Anatolian fault zone, *Tectonophysics*, **424**(3-4), 271–289.
- Manga, M., Beresnev, I., Brodsky, E. E., Elkhoury, J. E., Elsworth, D., Ingebritsen, S. E., Mays, D. C., & Wang, C.-Y., 2012. Changes in permeability caused by transient stresses: Field observations, experiments, and mechanisms, *Reviews of Geophysics*, **50**(2).
- Metzger, S., Schurr, B., Ratschbacher, L., Sudhaus, H., Kufner, S.-K., Schöne, T., Zhang, Y., Perry, M., & Bendick, R., 2017. The 2015 mw7.2 Sarez strike-slip Earthquake in the Pamir interior: Response to the underthrusting of India's western promontory, *Tectonics*, **36**(11), 2407–2421.
- Metzger, S., Ischuk, A., Deng, Z., Ratschbacher, L., Perry, M., Kufner, S.-K., Bendick, R., & Moreno, M., 2020. Dense GNSS profiles across the northwestern tip of the India-Asia collision zone: Triggered slip and westward flow of the Peter the First Range, Pamir, into the Tajik Depression, *Tectonics*, **39**(2), e2019TC005797.
- Michael, A. J., 1984. Determination of stress from slip data: faults and folds, *Journal of Geophysical Research: Solid Earth*, **89**(B13), 11517–11526.
- Michael, A. J., 1987. Use of focal mechanisms to determine stress: a control study, *Journal of Geophysical Research: Solid Earth*, **92**(B1), 357–368.
- Michele, M., Chiaraluce, L., Di Stefano, R., & Waldhauser, F., 2020. Fine-scale structure of the 2016–2017 Central Italy seismic sequence from data recorded at the Italian National Network, *Journal of Geophysical Research: Solid Earth*, **125**(4), e2019JB018440.
- Mildon, Z. K., Roberts, G. P., Walker, J. P. F., & Iezzi, F., 2017. Coulomb stress transfer and fault interaction over millennia on non-planar active normal faults: the Mw 6.5–5.0 seismic sequence of 2016–2017, central Italy, *Geophysical Journal International*, **210**(2), 1206–1218.
- Mildon, Z. K., Roberts, G. P., Walker, J. F., & Toda, S., 2019. Coulomb pre-stress and fault bends are ignored yet vital factors for earthquake triggering and hazard, *Nature communications*, **10**(1), 1–9.
- Miller, S. A., 2020. Aftershocks are fluid-driven and decay rates controlled by permeability dynamics, *Nature Communications*, **11**(1), 5787.
- Miller, S. A. & Nur, A., 2000. Permeability as a toggle switch in fluid-controlled crustal processes, *Earth and Planetary Science Letters*, **183**(1-2), 133–146.
- Morishita, Y., Lazecky, M., Wright, T. J., Weiss, J. R., Elliott, J. R., & Hooper, A., 2020. LiCSBAS: An open-source InSAR time series analysis package integrated with the LiCSAR automated Sentinel-1 InSAR processor, *Remote Sensing*, **12**(3), 424.
- Nábělek, J. & Xia, G., 1995. Moment-tensor analysis using regional data: Application to the 25 March, 1993, Scotts Mills, Oregon, Earthquake, *Geophysical Research Letters*, **22**(1), 13–16.
- Nalbant, S. S., Steacy, S., Sieh, K., Natawidjaja, D., & McCloskey, J., 2005. Earthquake risk on the Sunda trench, *Nature*, **435**(7043), 756–757.
- Nöth, L., 1932. *Geologische Untersuchungen im nordwestlichen Pamirgebiet und mittleren Transalai*,

Verlag Dietrich Reimer, Ernst Vohsen.

- Ogwari, P. & Horton, S., 2016. Numerical model of pore-pressure diffusion associated with the initiation of the 2010–2011 Guy–Greenbrier, Arkansas earthquakes, *Geofluids*, **16**(5), 954–970.
- Okada, Y., 1985. Surface deformation due to shear and tensile faults in a half-space, *Bulletin of the Seismological Society of America*, **75**(4), 1135–1154.
- Parsons, T. & Dreger, D. S., 2000. Static-stress impact of the 1992 Landers earthquake sequence on nucleation and slip at the site of the 1999 m=7.1 Hector Mine earthquake, southern California, *Geophysical Research Letters*, **27**(13), 1949–1952.
- Perfettini, H., Stein, R. S., Simpson, R., & Cocco, M., 1999. Stress transfer by the 1988–1989 Mw = 5.3 and 5.4 Lake Elsman foreshocks to the Loma Prieta fault: Unclamping at the site of peak mainshock slip, *Journal of Geophysical Research: Solid Earth*, **104**(B9), 20169–20182.
- Perry, M., Kakar, N., Ischuk, A., Metzger, S., Bendick, R., Molnar, P., & Mohadjer, S., 2019. Little geodetic evidence for localized Indian subduction in the Pamir-Hindu Kush of Central Asia, *Geophysical Research Letters*, **46**(1), 109–118.
- PMP International (Tajikistan), 2005. *Tajikistan National Seismic Network*.
- Pollitz, F. F., Banerjee, P., Bürgmann, R., Hashimoto, M., & Choosakul, N., 2006. Stress changes along the sunda trench following the 26 december 2004 sumatra-andaman and 28 march 2005 nias earthquakes, *Geophysical Research Letters*, **33**(6).
- Pozzi, J.-P. & Feinberg, H., 1991. Paleomagnetism in the Tajikistan: Continental shortening of European margin in the Pamirs during Indian Eurasian collision, *Earth and Planetary Science Letters*, **103**(1-4), 365–378.
- Qiao, X., Wang, Q., Yang, S., Li, J., Zou, R., & Ding, K., 2015. The 2008 Nura Mw6. 7 earthquake: A shallow rupture on the Main Pamir Thrust revealed by GPS and InSAR, *Geodesy and Geodynamics*, **6**(2), 91–100.
- Rice, J. R. & Cleary, M. P., 1976. Some basic stress diffusion solutions for fluid-saturated elastic porous media with compressible constituents, *Reviews of Geophysics*, **14**(2), 227–241.
- Robinson, A. C., 2009. Geologic offsets across the northern Karakorum fault: Implications for its role and terrane correlations in the western Himalayan-Tibetan orogen, *Earth and Planetary Science Letters*, **279**(1-2), 123–130.
- Robinson, A. C., Yin, A., Manning, C. E., Harrison, T. M., Zhang, S.-H., & Wang, X.-F., 2004. Tectonic evolution of the northeastern Pamir: Constraints from the northern portion of the Cenozoic Kongur Shan extensional system, western China, *Geological Society of America Bulletin*, **116**(7-8), 953–973.
- Robinson, A. C., Yin, A., Manning, C. E., Harrison, T. M., Zhang, S.-H., & Wang, X.-F., 2007. Cenozoic evolution of the eastern Pamir: Implications for strain-accommodation mechanisms at the western end of the Himalayan-Tibetan orogen, *Geological Society of America Bulletin*, **119**(7-8), 882–896.

- Rutte, D., Ratschbacher, L., Schneider, S., Stübner, K., Stearns, M. A., Gulzar, M. A., & Hacker, B. R., 2017. Building the Pamir-Tibetan Plateau—Crustal stacking, extensional collapse, and lateral extrusion in the Central Pamir: 1. Geometry and kinematics, *Tectonics*, **36**(3), 342–384.
- Ryder, I., Bürgmann, R., & Fielding, E., 2012. Static stress interactions in extensional earthquake sequences: An example from the south lunggar rift, tibet, *Journal of Geophysical Research: Solid Earth*, **117**(B9).
- Sangha, S., Peltzer, G., Zhang, A., Meng, L., Liang, C., Lundgren, P., & Fielding, E., 2017. Fault geometry of 2015, Mw7.2 Murghab, Tajikistan earthquake controls rupture propagation: Insights from InSAR and seismological data, *Earth and Planetary Science Letters*, **462**, 132–141.
- Sass, P., Ritter, O., Ratschbacher, L., Tympel, J., Matiukov, V., Rybin, A., & Batalev, V. Y., 2014. Resistivity structure underneath the Pamir and southern Tian Shan, *Geophysical Journal International*, **198**(1), 564–579.
- Schneider, F., Yuan, X., Schurr, B., Mechie, J., Sippl, C., Haberland, C., Minaev, V., Oimahmadov, I., Gadoev, M., Radjabov, N., et al., 2013. Seismic imaging of subducting continental lower crust beneath the Pamir, *Earth and Planetary Science Letters*, **375**, 101–112.
- Schurr, B., Ratschbacher, L., Sippl, C., Gloaguen, R., Yuan, X., & Mechie, J., 2014. Seismotectonics of the Pamir, *Tectonics*, **33**(8), 1501–1518.
- Schurr, B., Moreno, M., Tréhu, A. M., Bedford, J., Kummerow, J., Li, S., & Oncken, O., 2020. Forming a Mogi doughnut in the years prior to and immediately before the 2014 M8.1 Iquique, northern Chile, earthquake, *Geophysical Research Letters*, **47**(16), e2020GL088351.
- SEISDMC, 2021. Data management centre of the China National Seismic Network at the Institute of Geophysics, *China Earthquake Administration*.
- Shapiro, S. A., Huenges, E., & Borm, G., 1997. Estimating the crust permeability from fluid-injection-induced seismic emission at the KTB site, *Geophysical Journal International*, **131**(2), F15–F18.
- Shapiro, S. A., Patzig, R., Rothert, E., & Rindschwentner, J., 2003. Triggering of seismicity by pore-pressure perturbations: Permeability-related signatures of the phenomenon, in *Thermo-Hydro-Mechanical Coupling in Fractured Rock*, pp. 1051–1066, Birkhäuser Basel.
- Sibson, R., 1992. Implications of fault-valve behaviour for rupture nucleation and recurrence, *Tectonophysics*, **211**(1-4), 283–293.
- Sippl, C., Schurr, B., Tympel, J., Angiboust, S., Mechie, J., Yuan, X., Schneider, F., Sobolev, S. V., Ratschbacher, L., Haberland, C., et al., 2013a. Deep burial of Asian continental crust beneath the Pamir imaged with local earthquake tomography, *Earth and Planetary Science Letters*, **384**, 165–177.
- Sippl, C., Schurr, B., Yuan, X., Mechie, J., Schneider, F., Gadoev, M., Orunbaev, S., Oimahmadov, I., Haberland, C., Abdybachaev, U., et al., 2013b. Geometry of the Pamir-Hindu Kush intermediate-depth earthquake zone from local seismic data, *Journal of Geophysical Research: Solid Earth*, **118**(4), 1438–

1457.

- Sippl, C., Ratschbacher, L., Schurr, B., Krumbiegel, C., Rui, H., Pingren, L., & Abdybachaev, U., 2014. The 2008 Nura earthquake sequence at the Pamir-Tian Shan collision zone, southern Kyrgyzstan, *Tectonics*, **33**(12), 2382–2399.
- Sobel, E. R., Schoenbohm, L. M., Chen, J., Thiede, R., Stockli, D. F., Sudo, M., & Strecker, M. R., 2011. Late Miocene–Pliocene deceleration of dextral slip between Pamir and Tarim: Implications for Pamir orogenesis, *Earth and Planetary Science Letters*, **304**(3-4), 369–378.
- Stein, R. S., 1999. The role of stress transfer in earthquake occurrence, *Nature*, **402**(6762), 605–609.
- Strecker, M., Frisch, W., Hamburger, M., Ratschbacher, L., Semiletkin, S., Zamoruyev, A., & Sturchio, N., 1995. Quaternary deformation in the eastern Pamirs, Tadzhikistan and Kyrgyzstan, *Tectonics*, **14**(5), 1061–1079.
- Strom, A., 2014. Sarez Lake problem: ensuring long-term safety, in *Landslide Science for a Safer Geoenvironment*, pp. 633–639, Springer.
- Stübner, K., Ratschbacher, L., Rutte, D., Stanek, K., Minaev, V., Wiesinger, M., Gloaguen, R., & members, P. T., 2013. The giant Shakh dara migmatitic gneiss dome, Pamir, India-Asia collision zone: 1. Geometry and kinematics, *Tectonics*, **32**(4), 948–979.
- Tanaka, S., Ohtake, M., & Sato, H., 2002. Evidence for tidal triggering of earthquakes as revealed from statistical analysis of global data, *Journal of Geophysical Research: Solid Earth*, **107**(B10), ESE–1.
- Teshebaeva, K., Sudhaus, H., Echtler, H., Schurr, B., & Roessner, S., 2014. Strain partitioning at the eastern Pamir-Alai revealed through SAR data analysis of the 2008 Nura earthquake, *Geophysical Journal International*, **198**(2), 760–774.
- Thiede, R. C., Sobel, E. R., Chen, J., Schoenbohm, L. M., Stockli, D. F., Sudo, M., & Strecker, M. R., 2013. Late Cenozoic extension and crustal doming in the India-Eurasia collision zone: New thermochronologic constraints from the NE Chinese Pamir, *Tectonics*, **32**(3), 763–779.
- Thomas, J.-C., Chauvin, A., Gapais, D., Bazhenov, M., Perroud, H., Cobbold, P., & Burtman, V., 1994. Paleomagnetic evidence for Cenozoic block rotations in the Tadjik depression (Central Asia), *Journal of Geophysical Research: Solid Earth*, **99**(B8), 15141–15160.
- Thurber, C. H., 1983. Earthquake locations and three-dimensional crustal structure in the Coyote Lake area, central California, *Journal of Geophysical Research: Solid Earth*, **88**(B10), 8226–8236.
- Toda, S. & Stein, R. S., 2020. Long- and short-term stress interaction of the 2019 Ridgecrest sequence and Coulomb-based earthquake forecasts, *Bulletin of the Seismological Society of America*, **110**(4), 1765–1780.
- Toda, S., Stein, R. S., Reasenber, P. A., Dieterich, J. H., & Yoshida, A., 1998. Stress transferred by the 1995 Mw=6.9 Kobe, Japan, shock: Effect on aftershocks and future earthquake probabilities, *Journal of Geophysical Research: Solid Earth*, **103**(B10), 24543–24565.

- Valoroso, L., Chiaraluce, L., Piccinini, D., Di Stefano, R., Schaff, D., & Waldhauser, F., 2013. Radiography of a normal fault system by 64,000 high-precision earthquake locations: The 2009 L'Aquila (central Italy) case study, *Journal of Geophysical Research: Solid Earth*, **118**(3), 1156–1176.
- Waldhauser, F. & Ellsworth, W. L., 2000. A double-difference earthquake location algorithm: Method and application to the northern Hayward fault, California, *Bulletin of the Seismological Society of America*, **90**(6), 1353–1368.
- Wang, R., Lorenzo-Martin, F., & Roth, F., 2006. PSGRN/PSCMP—a new code for calculating co-and post-seismic deformation, geoid and gravity changes based on the viscoelastic-gravitational dislocation theory, *Computers & Geosciences*, **32**(4), 527–541.
- Wells, D. L. & Coppersmith, K. J., 1994. New empirical relationships among magnitude, rupture length, rupture width, rupture area, and surface displacement, *Bulletin of the seismological Society of America*, **84**(4), 974–1002.
- Wessel, P., Smith, W. H., Scharroo, R., Luis, J., & Wobbe, F., 2013. Generic mapping tools: improved version released, *Eos, Transactions American Geophysical Union*, **94**(45), 409–410.
- Wiseman, K. & Burgmann, R., 2011. Stress and seismicity changes on the sunda megathrust preceding the 2007 mw 8.4 earthquake, *Bulletin of the Seismological Society of America*, **101**(1), 313–326.
- Woessner, J. & Wiemer, S., 2005. Assessing the quality of earthquake catalogues: Estimating the magnitude of completeness and its uncertainty, *Bulletin of the Seismological Society of America*, **95**(2), 684–698.
- Woo, J.-U., Kim, M., Sheen, D.-H., Kang, T.-S., Rhie, J., Grigoli, F., Ellsworth, W. L., & Giardini, D., 2019. An in-depth seismological analysis revealing a causal link between the 2017 m_w 5.5 pohang earthquake and EGS project, *Journal of Geophysical Research: Solid Earth*, **124**(12), 13060–13078.
- Worthington, J. R., Ratschbacher, L., Stübner, K., Khan, J., Malz, N., Schneider, S., Kapp, P., Chapman, J. B., Stevens Goddard, A., Brooks, H. L., et al., 2020. The Alichur dome, South Pamir, western India–Asia collisional zone: Detailing the Neogene Shakh dara–Alichur syn-collisional gneiss-dome complex and connection to lithospheric processes, *Tectonics*, **39**(1), e2019TC005735.
- Yadav, R., Gahalaut, V., Chopra, S., & Shan, B., 2012. Tectonic implications and seismicity triggering during the 2008 baluchistan, pakistan earthquake sequence, *Journal of Asian Earth Sciences*, **45**, 167–178.
- Yu, C., Li, Z., Penna, N. T., & Crippa, P., 2018. Generic atmospheric correction model for Interferometric Synthetic Aperture Radar observations, *Journal of Geophysical Research: Solid Earth*, **123**(10), 9202–9222.
- Yuan, X., Schurr, B., Bloch, W., Xu, Q., & Zhao, J., 2018a. East Pamir seismic network, *GFZ Data services*.
- Yuan, X., Schurr, B., Kufner, S.-K., & Bloch, W., 2018b. Sarez Pamir aftershock seismic network, *GFZ*

Data services.

- Yushin, I., Sass, M., Karapetov, S., Altukhov, S., Teplov, I., Raeakov, C., Harkov, S., & Davidchenko, A., 1964. *1: 200,000 maps of the Tajik SSR*, Russian Geological Research Institute, Nedra, Moscow.
- Zhou, Y., He, J., Oimahmadov, I., Gadoev, M., Pan, Z., Wang, W., Abdulov, S., & Rajabov, N., 2016. Present-day crustal motion around the Pamir Plateau from GPS measurements, *Gondwana Research*, **35**, 144–154.
- Ziv, A. & Rubin, A. M., 2000. Static stress transfer and earthquake triggering: No lower threshold in sight?, *Journal of Geophysical Research: Solid Earth*, **105**(B6), 13631–13642.
- Zubovich, A. V., Wang, X.-q., Scherba, Y. G., Schelochkov, G. G., Reilinger, R., Reigber, C., Mosienko, O. I., Molnar, P., Michajljow, W., Makarov, V. I., Li, J., Kuzikov, S. I., Herring, T. A., Hamburger, M. W., Hager, B. H., Dang, Y.-m., Bragin, V. D., & Beisenbaev, R. T., 2010. GPS velocity field for the Tien Shan and surrounding regions, *Tectonics*, **29**(6), TC6014.
- Zubovich, A. V., Schöne, T., Metzger, S., Mosienko, O., Mukhamediev, S., Sharshebaev, A., & Zech, C., 2016. Tectonic interaction between the Pamir and Tien Shan observed by GPS, *Tectonics*, **35**(2), 283–292.

Supplemental Material to:
The 2015–2017 Pamir Earthquake Sequence:
Fore-, Main-, and Aftershocks, Seismotectonics,
Fault Interaction, and Fluid Processes

Wasja Bloch^{1,2*}, Sabrina Metzger¹, Bernd Schurr¹, Xiaohui Yuan¹,
Lothar Ratschbacher³, Sanaa Reuter³, Qiang Xu^{4,5}, Junmeng Zhao^{4,5},
Shokhrukh Murodkulov⁶, Ilhomjon Oimuhammadzoda⁷

¹ *GFZ German Research Centre for Geosciences, 14473 Potsdam, Germany*

² *Department of Earth, Ocean and Atmospheric Sciences, University of British Columbia, Vancouver V6T 1Z4, Canada*

³ *Geologie, Technische Universität Bergakademie Freiberg, 09599 Freiberg, Germany*

⁴ *Key Laboratory of Continental Collision and Plateau Uplift, Institute of Tibetan Plateau Research, Chinese Academy of Sciences, Beijing 100101, China*

⁵ *CAS Center for Excellence in Tibetan Plateau Earth Sciences, Beijing 100101, China*

⁶ *Institute of Geology, Earthquake Engineering and Seismology, National Academy of Sciences, Dushanbe, Tajikistan*

⁷ *Department of Geology under the Government of the Republic of Tajikistan, Dushanbe, Tajikistan*

Contents of this file

(i) Video S1: Animated Map View of the Earthquake Sequence

(ii) Figs. S1 to S16

Additional Supporting Information (Files uploaded separately)

Video S1: Animated Map View on the Earthquake Sequence The video is an animated representation of Fig. 2a and b of the main text. Every audible "click" represents one seismic event, the gain scales linear with earthquake magnitude. The events fade out within 100 days.

REFERENCES

- Sipl, C., Schurr, B., Yuan, X., Mechie, J., Schneider, F., Gadoev, M., Orunbaev, S., Oimahmadov, I., Haberland, C., Abdybachaev, U., et al., 2013. Geometry of the Pamir-Hindu Kush intermediate-depth earthquake zone from local seismic data, *Journal of Geophysical Research: Solid Earth*, **118**(4), 1438–1457.
- Utsu, T., Ogata, Y., et al., 1995. The centenary of the Omori formula for a decay law of aftershock activity, *Journal of Physics of the Earth*, **43**(1), 1–33.

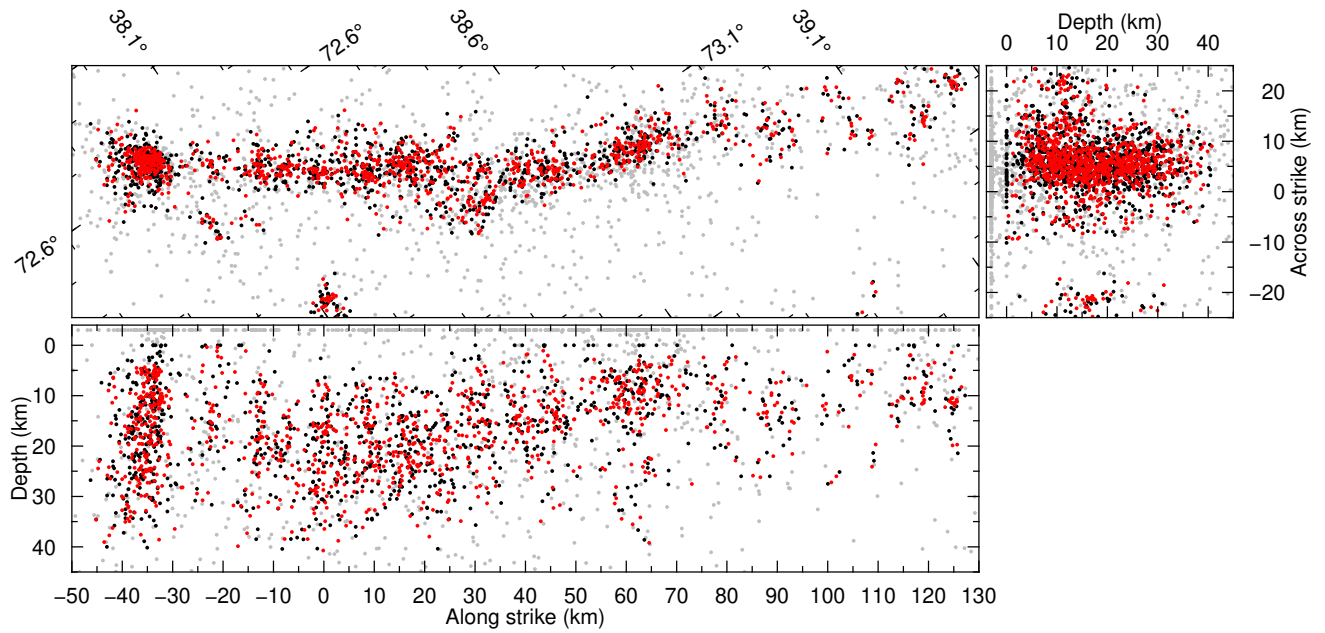


Figure S1. Comparison of event locations for the Sarez earthquake (Fig. 4 of the main text) after the different steps of the event location. Center panel: Map view. Right panel: across-strike profile. Lower panel: along-strike profile. Gray dots are hypocenters which could only be located with *simulps*, but not re-located. Black dots are hypocenters before and red dots after the re-location with *hypoDD*.

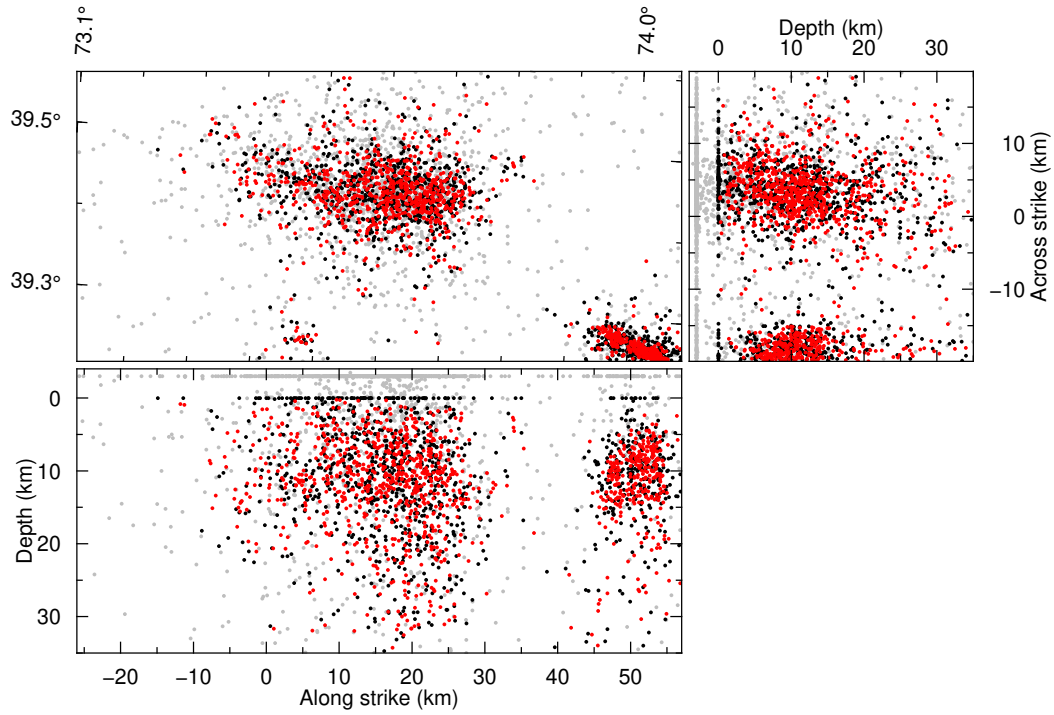


Figure S2. As Fig. S1, but for the Sary-Tash earthquake (Fig. 6 of the main text).

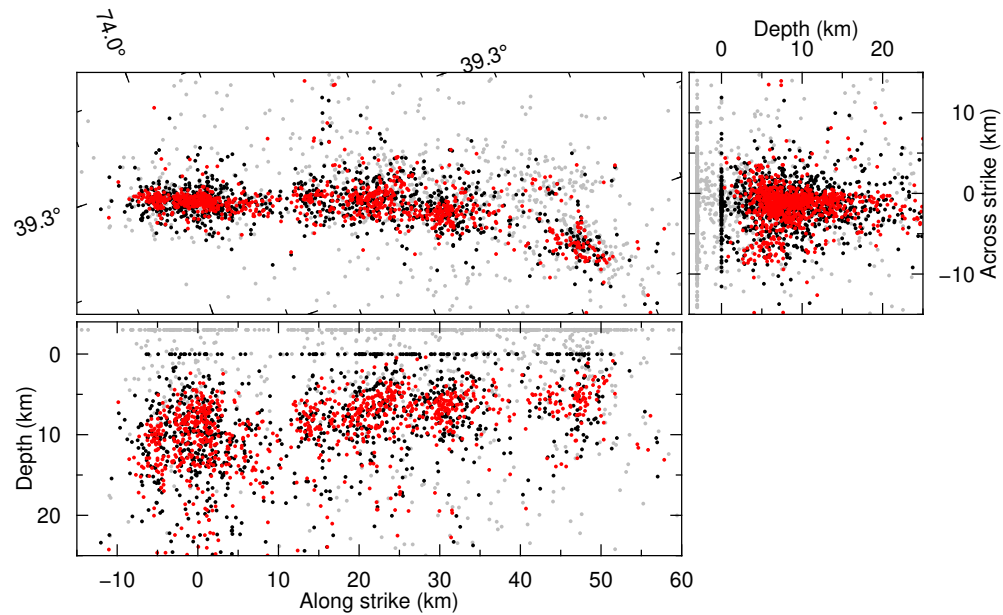


Figure S3. As Fig. S1, but for the Muji earthquake (Fig. 7 of the main text).

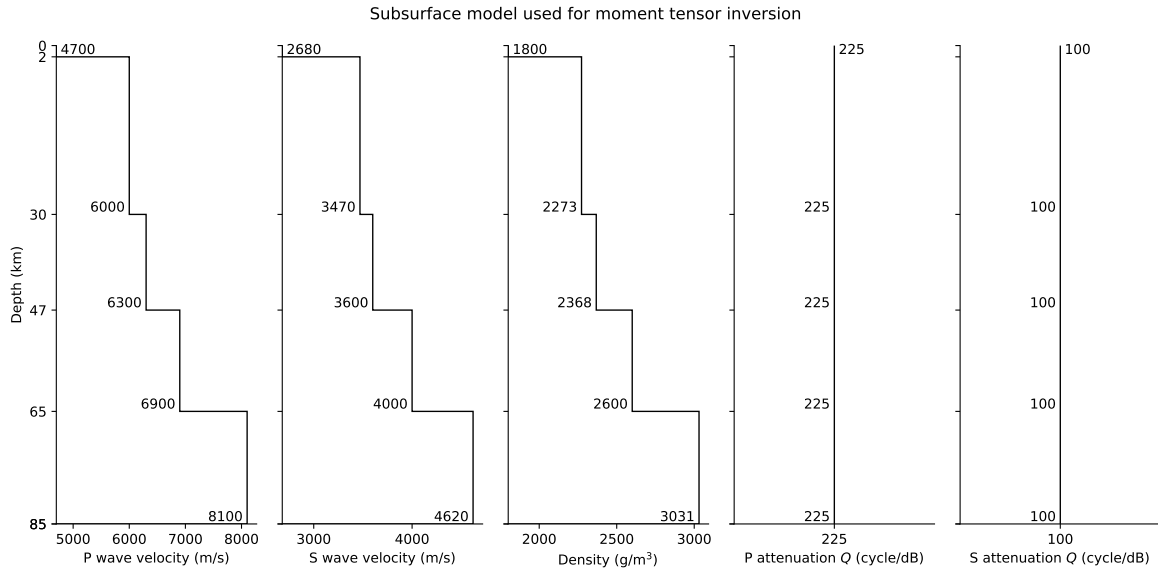


Figure S4. Subsurface model (Sippl et al. 2013) used for the determination of regional moment tensors.

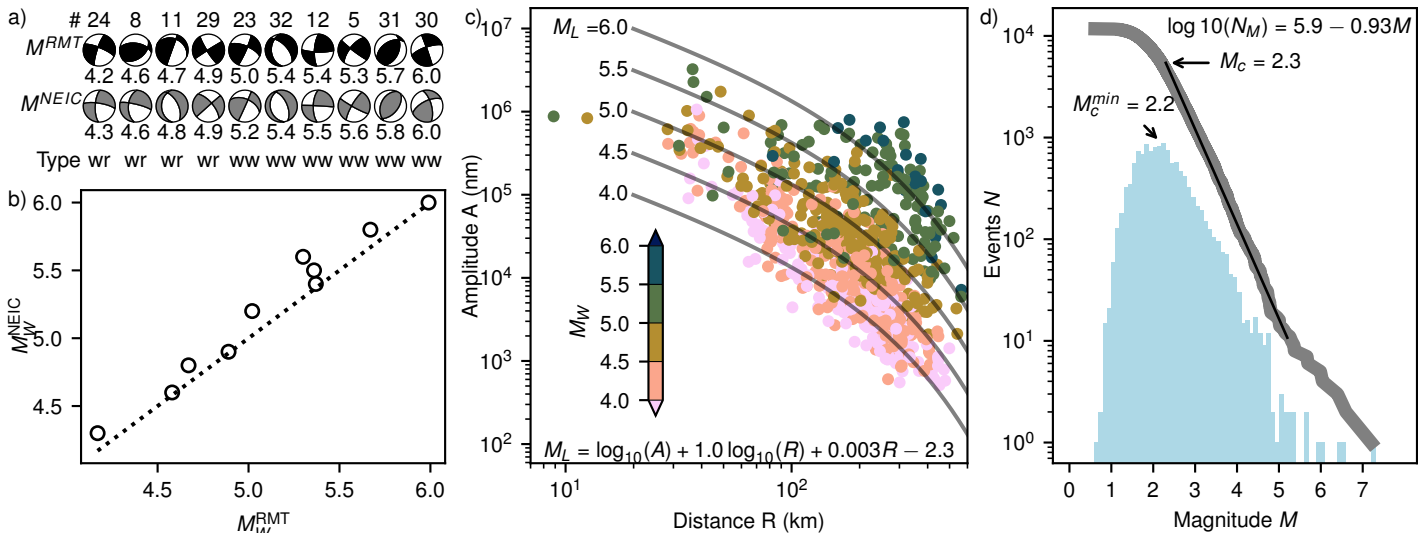


Figure S5. Moment magnitudes of seismic events. Comparison of regional moment tensors (a) and magnitudes (b) with results by NEIC. (wr) regional (ww) W-phase. (c) Calibration of local magnitudes with parameters of Equation 1 of the main text. (d) Magnitude distribution of the entire catalog. Completeness magnitude M_C , and most frequent magnitude M_C^{min} .

160627_0625, 16/ 6/27 6:25:36 $M_w=4.6$ 20-60s 12km DC:77%

Z

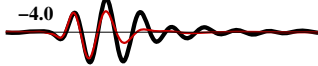
R

T

EP04
57° 92 km



EP03
75° 119 km



EP02
75° 189 km



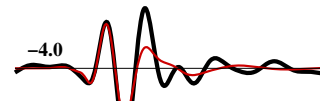
EP07
93° 129 km



EP19
99° 243 km



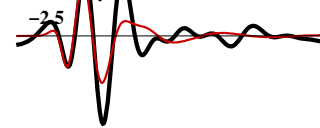
EP11
103° 187 km



EP10
114° 81 km



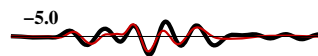
EP08
118° 96 km



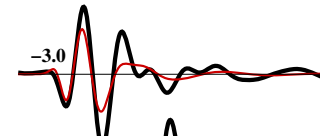
EP21
119° 255 km



EP28
126° 289 km



EP09
133° 80 km



EP30
135° 280 km



CHE6
157° 129 km



P146
175° 78 km



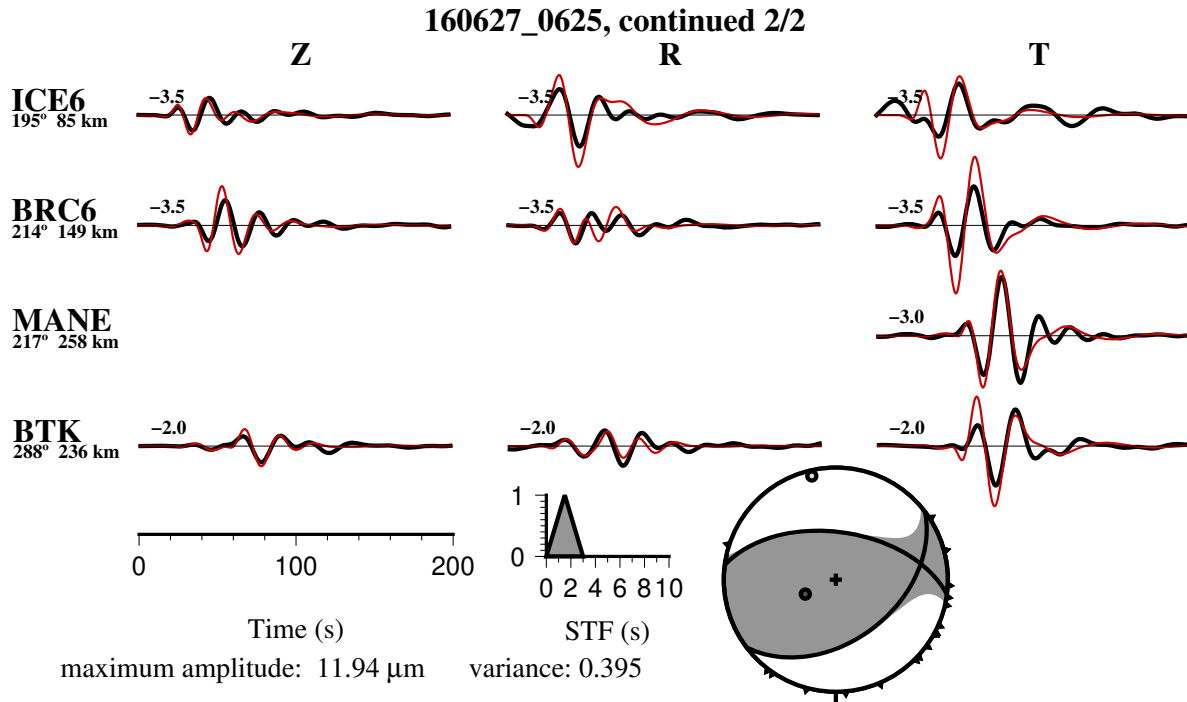
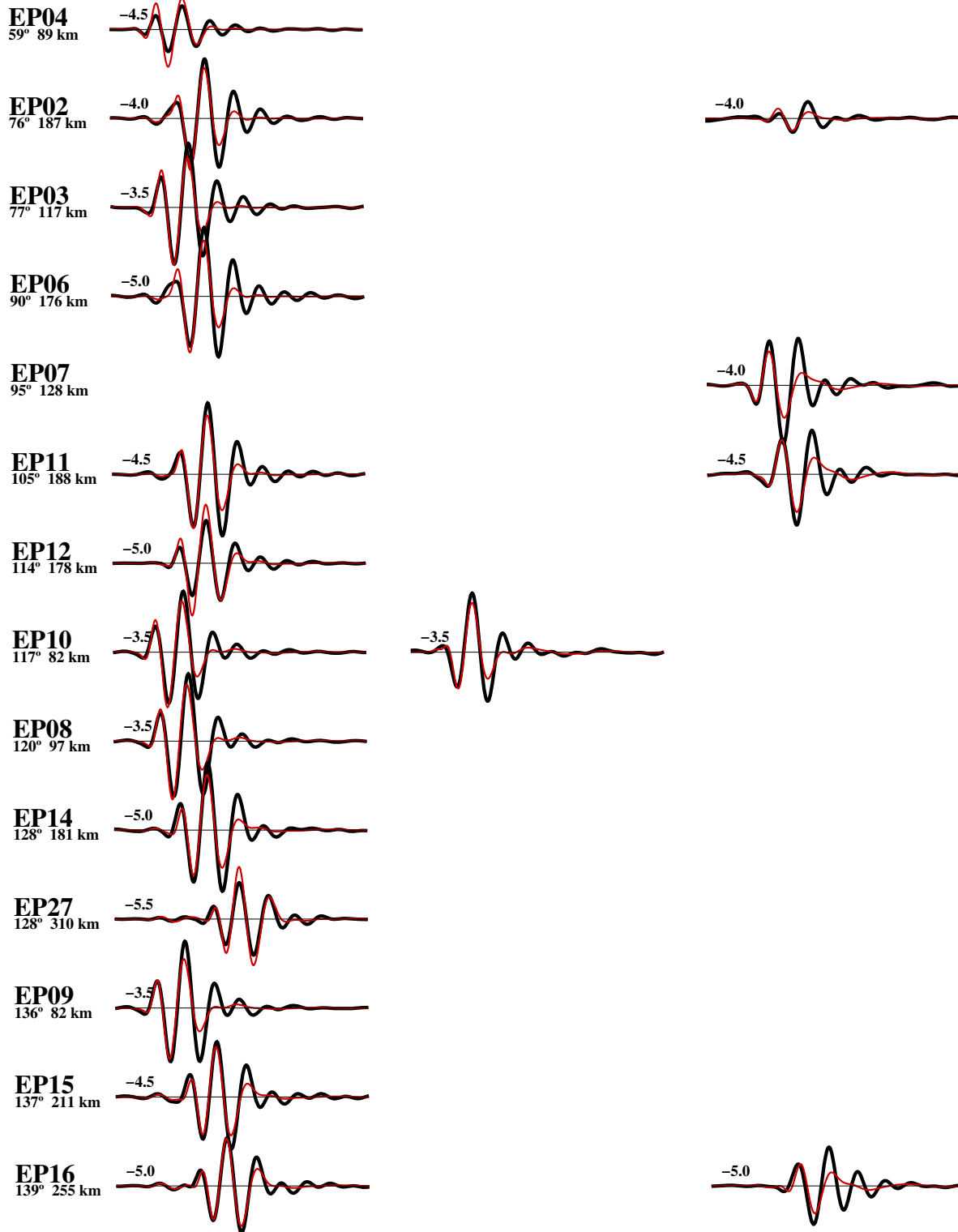


Figure S6. Results of moment tensor inversion for event 8 (Fig. S5), with observed (black) and modeled (red) waveforms for vertical (Z), radial (R) and transverse (T) component on the stations named on the left. Event back-azimuth and distance given below station name.

160628_1243, 16/ 6/28 12:43:13 $M_w=4.7$ 20-60s 15km DC:81%
Z R T



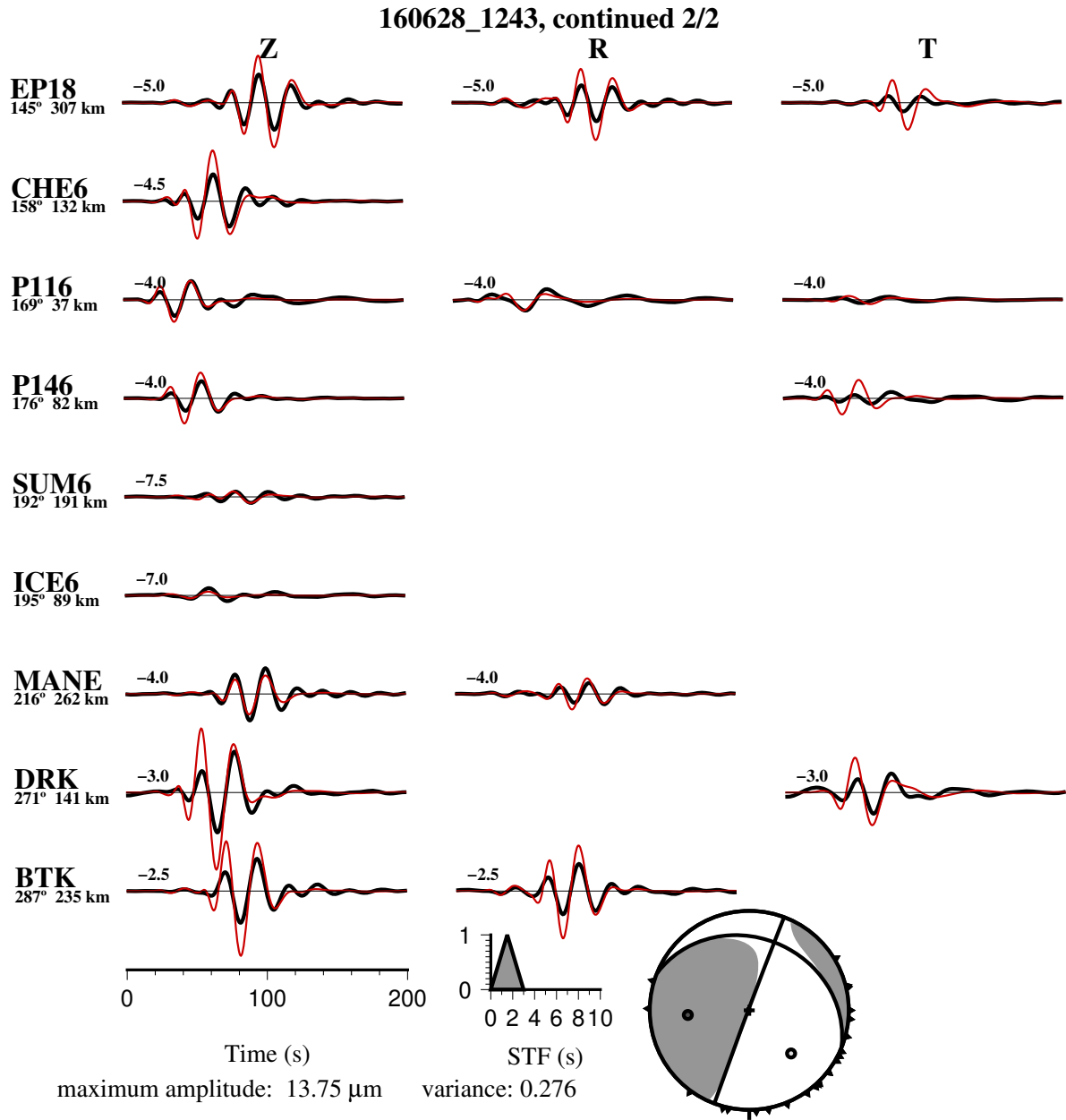


Figure S7. As Fig. S6, but for event 11 (Fig. S5).

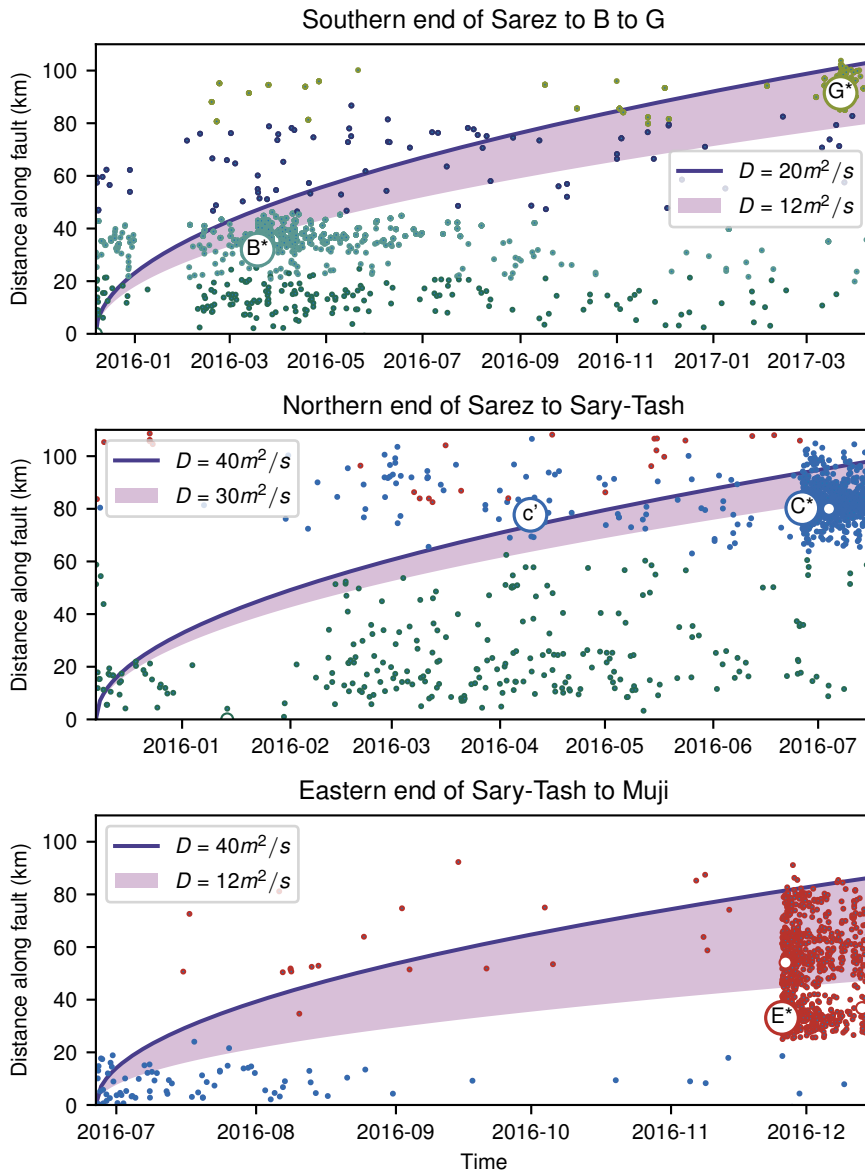


Figure S8. Spatio-temporal evolution of seismicity along the (top) southern continuation of the SKFS; (middle) northern continuation of the SKFS; (bottom) continuation of the MPTS into the Muji fault. D according to Equation 8 of the main text.

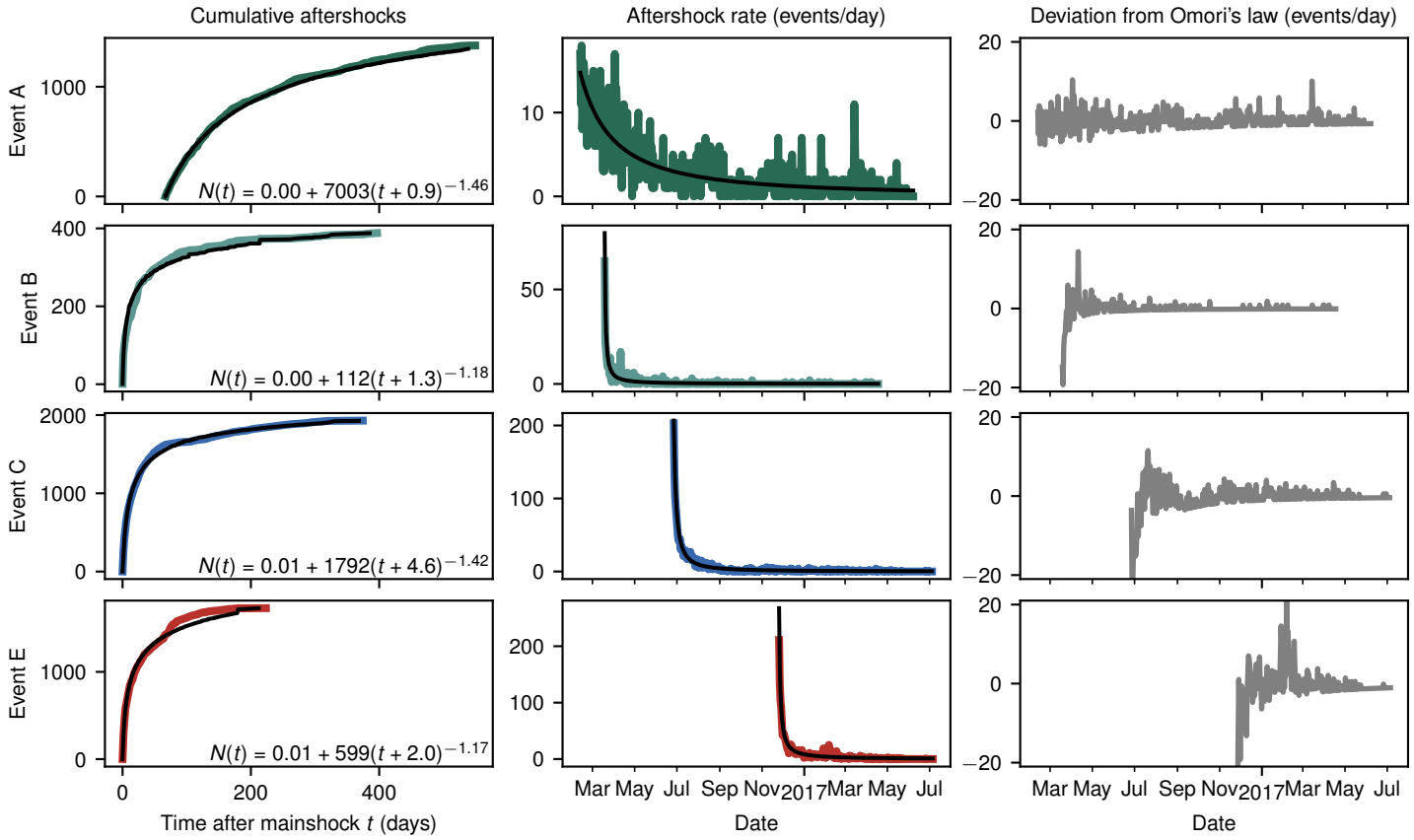


Figure S9. Aftershock characteristics of mainshock vicinities *A*, *B*, *C*, and *E*. Left column: Cumulative aftershocks after the mainshock (*A** only shown after installation of 8H network) and parameters of modified Omori's Law (Utsu et al. 1995). Middle column: Aftershock rate over time. Right column: Deviation of aftershock rate from Omori's law over time. Even though time intervals of increased aftershock activity exist, they do not correlate with each other in between earthquake sequences.

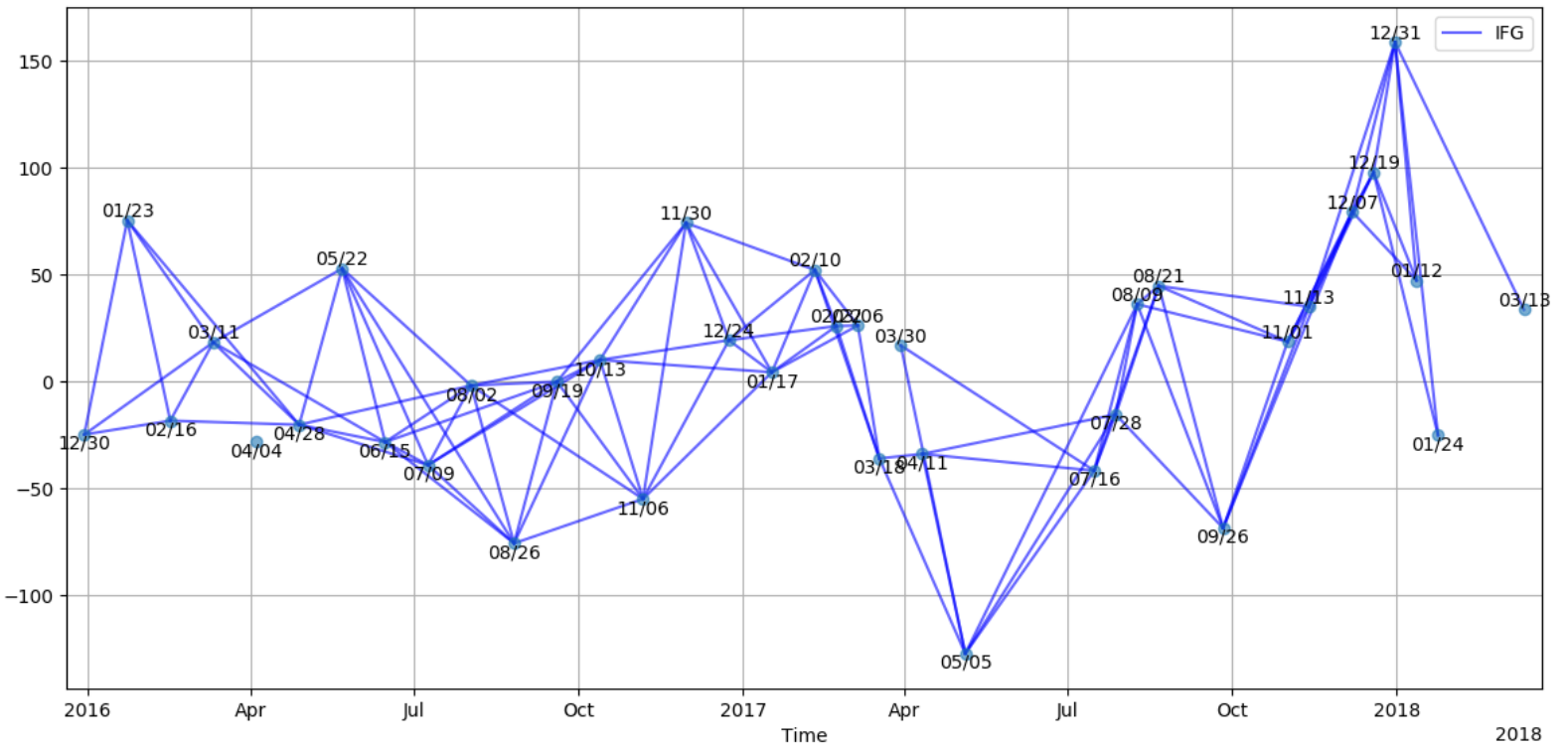


Figure S10. Perpendicular baseline (Bperp) against time for InSAR frame 100A.052 (Figs. 4 and S12). Lines indicate combination of acquired images to compute differential interferograms.

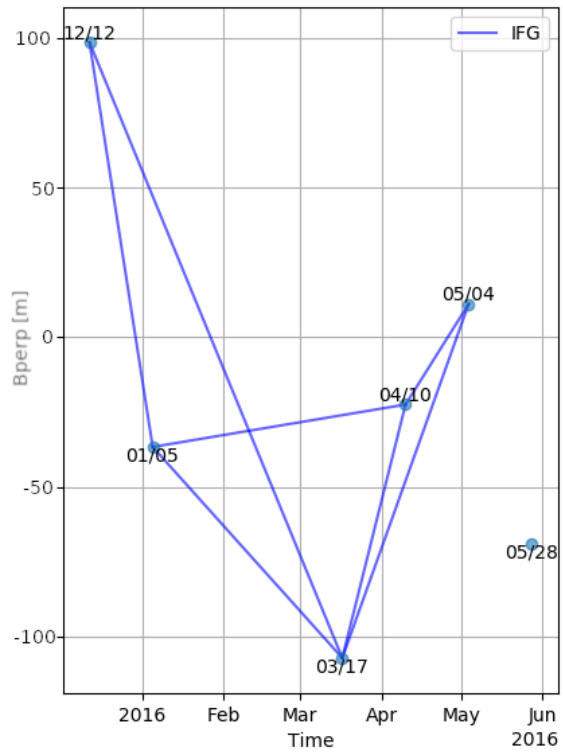


Figure S11. As Fig. S10, but for frame 005D.050.

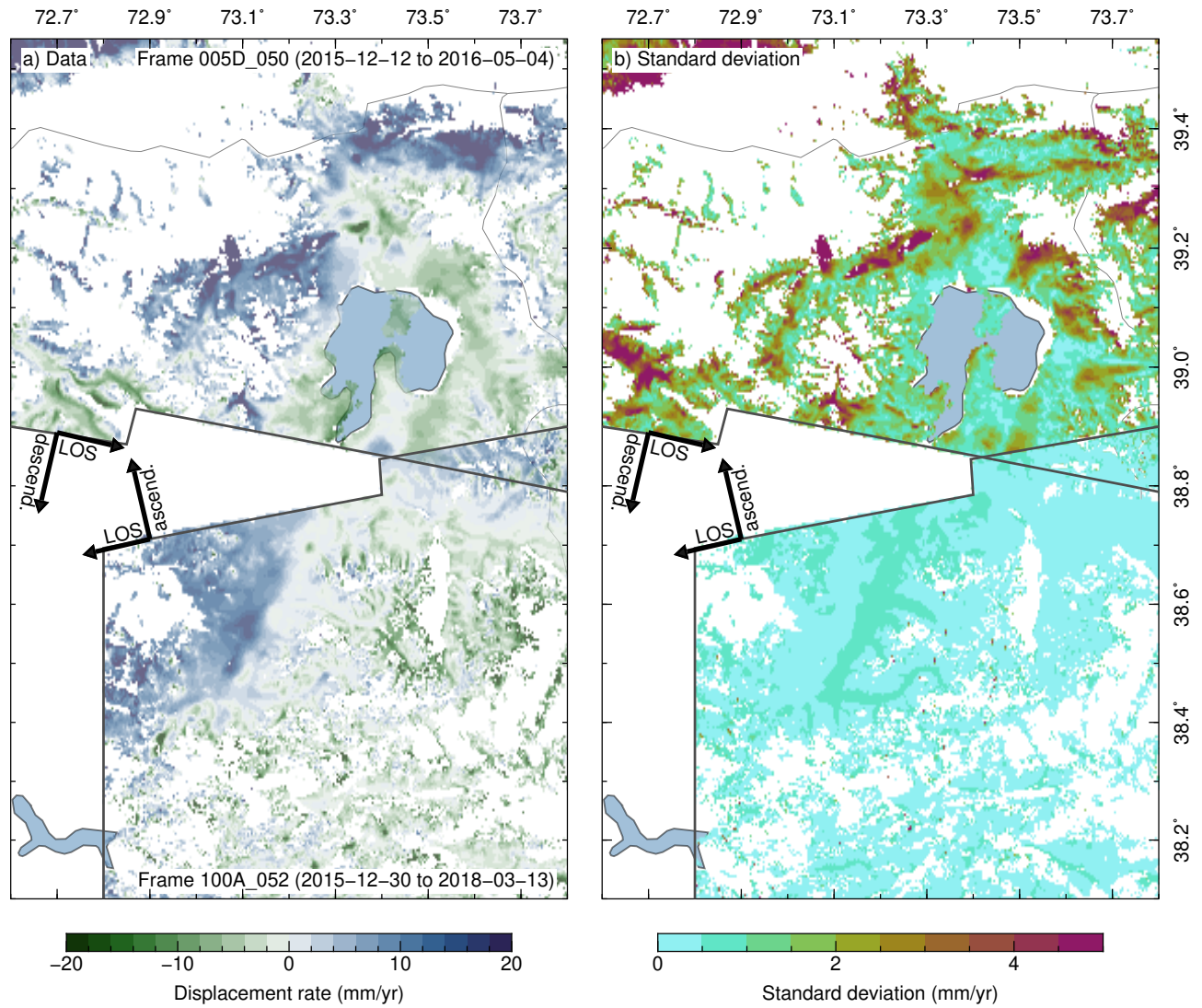


Figure S12. InSAR time series as in Fig. 5 of the main text. Left: rate map before conversion to displacement. Right: Nominal uncertainty of displacement rate.

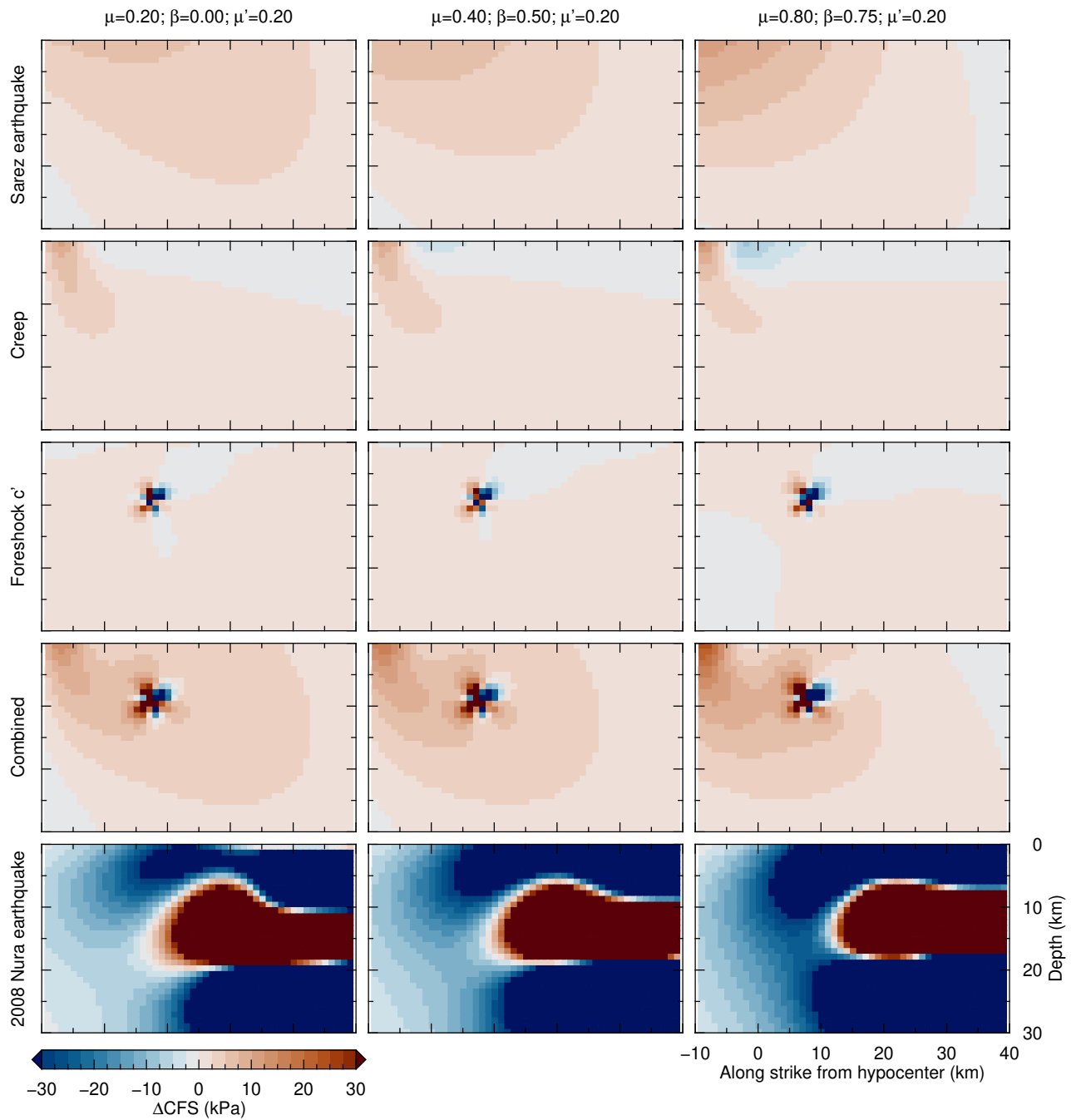


Figure S13. Contributions of distinct stress sources to the change in Coulomb failure stress (ΔCFS) on the fault plane of the Sary-Tash earthquake in dependence of friction (μ) and Skempton's parameter (β) under constant apparent friction (μ').

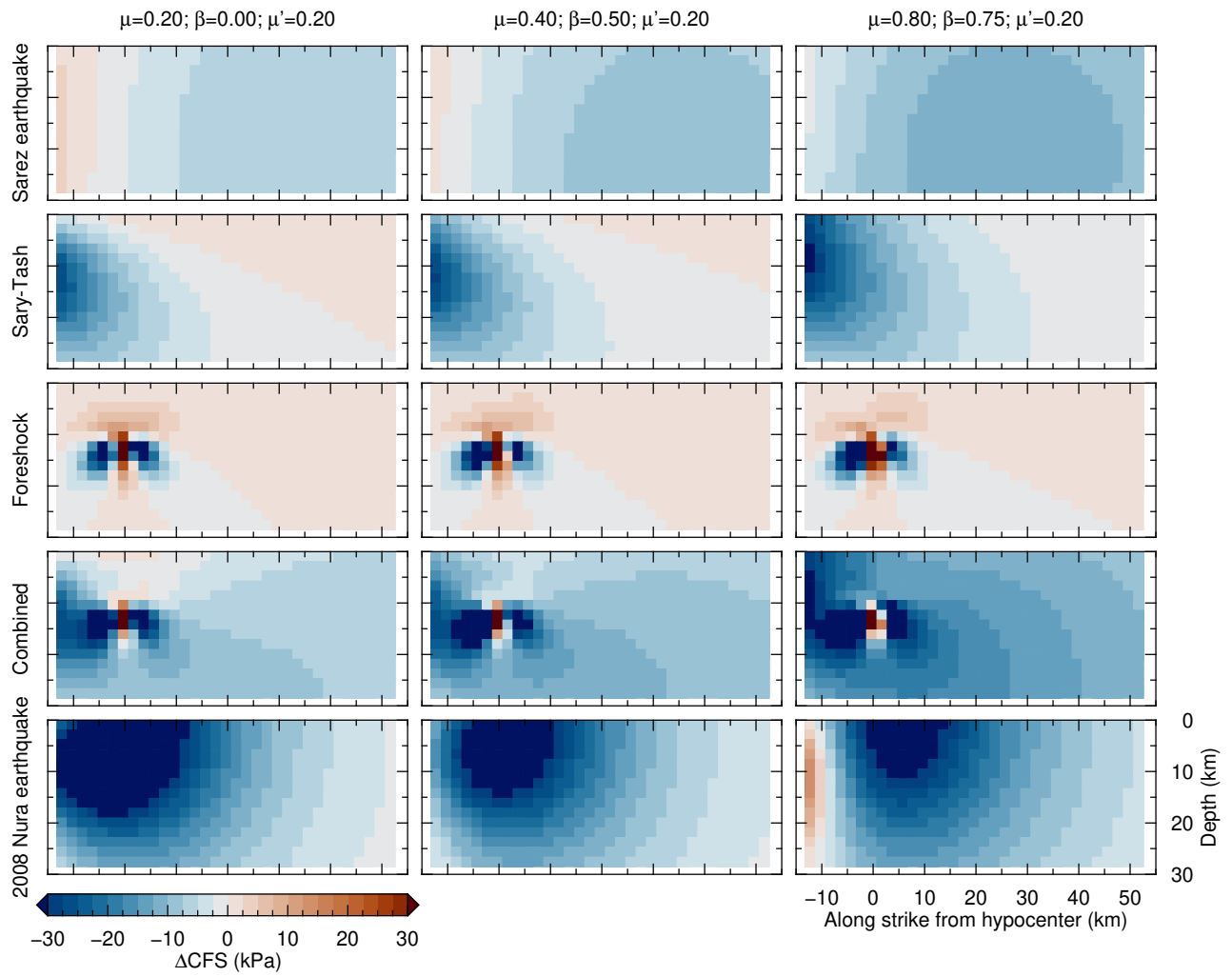


Figure S14. As Fig. S13, but for the Muji earthquake.

Δ CFS at Sary-Tash hypocenter C: $+5^{+4}_{-3}$ kPa

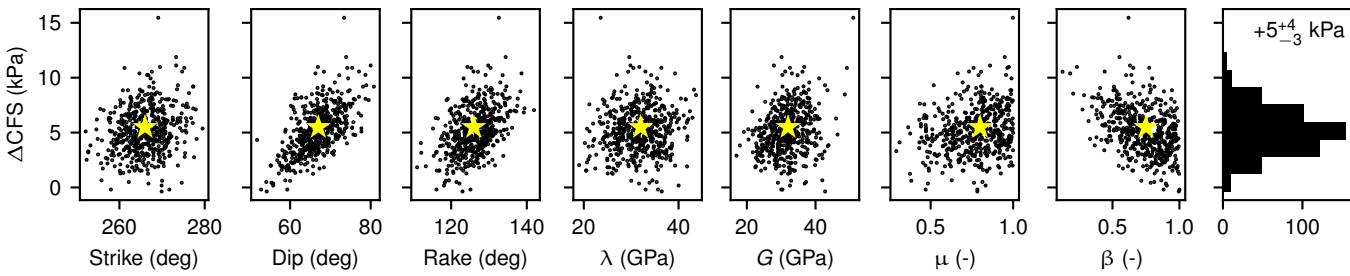


Figure S15. Sensitivity analysis of Coulomb failure stress changes at the Sary-Tash hypocenter C^* due to the Sarez earthquake, postseismic slip on the Sarez fault and foreshock e' . Contributions (from left to right) of normal distributed variations around the preferred values (stars) of receiver fault's strike, dip and rake (with a standard deviation of 5°), Lamé's parameters λ and G (standard deviation of 5 GPa), friction coefficient μ , and Skempton's parameter β (standard deviation 0.2, ensuring [0, 1] range). Resulting median, 5% and 95% quantiles under the assumption of input uncertainties.

Δ CFS at Muji hypocenter E and Muji foreshock e' : -18^{+9}_{-9} kPa

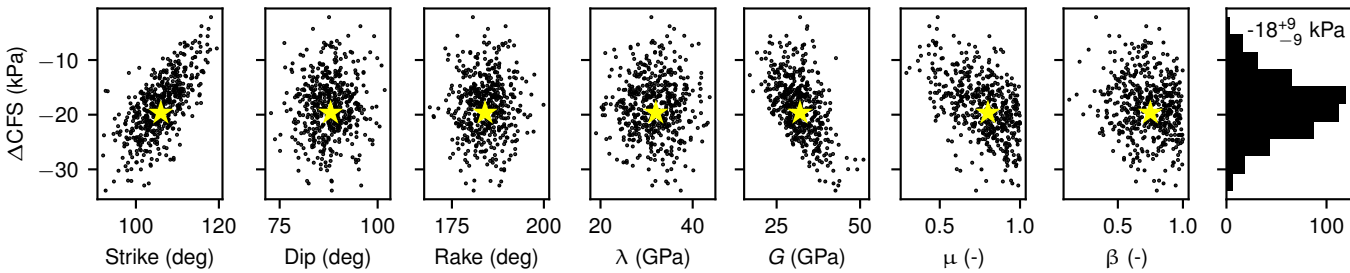


Figure S16. Sensitivity analysis of Coulomb failure stress changes as in Fig. S15, but due to the Sarez and Sary-Tash earthquakes at the Muji mainshock E^* or Muji foreshock e' hypocenter, both of which yield the same results within 100 Pa.